International Journal of Solids and Structures 207 (2020) 206–229

Contents lists available at ScienceDirect

International Journal of Solids and Structures

journal homepage: www.elsevier.com/locate/ijsolstr

Exact axisymmetric adhesive contact analysis for a pre-deformed soft electroactive half-space

Guozhan Xia [a,b], Yilan Huang [a,b], Yipin Su [a,c], Weiqiu Chen [a,b,d,*]

[a] Key Laboratory of Soft Machines and Smart Devices of Zhejiang Province & Department of Engineering Mechanics, Zhejiang University, Hangzhou 310027, PR China
[b] State Key Laboratory of CAD & CG, Zhejiang University, Hangzhou 310058, PR China
[c] School of Mathematics, Statistics and Applied Mathematics, NUI Galway, University Road, Galway, Ireland
[d] Soft Matter Research Center, Zhejiang University, Hangzhou 310027, PR China

ARTICLE INFO

Article history:
Received 18 March 2020
Received in revised form 6 August 2020
Accepted 28 September 2020
Available online 9 October 2020

Keywords:
Soft electroactive material
Contact theory
Adhesive effect
Surface instability

ABSTRACT

In this paper, three-dimensional exact solutions of adhesive contact between a pre-deformed compressible soft electroactive half-space and an axisymmetric rigid indenter are presented. The change of surface adhesion energy during the contact is examined by using the modified JKR model, which accounts for the real contact area instead of the projected area. With the help of new results in the potential theory method, all physical (field) variables are derived in terms of elementary functions for three common types of axisymmetric indenters (flat-ended, conical, and spherical). The analytical contact relations for different indenter geometries and material properties are provided and summarized in Tables 2 and 3 to serve a solid base for revealing the underlying electromechanical mechanism of soft electroactive materials. For numerical illustration, neo-Hookean isotropic electroactive material is considered. The simulation results clearly demonstrate that both the mechanical and electric biasing fields significantly affect the indentation measurement of the electroactive material. Moreover, at either micro- or nano-scale, adhesion plays a prominent role in the indentation responses. It is of interest that, even without adhesion, the normal stress somewhere in the contact region may become tensile under a prescribed pre-stretch when the biasing electric displacement exceeds a certain value. This abnormal phenomenon actually corresponds to surface instability of the half-space under the biasing field. In the case of adhesive contact, other than the surface instability, the value of surface adhesion energy between the probe and the sample will impose a constraint on the validity of indentation analysis within the linear elastic regime.

1. Introduction

Since the early 1990s, soft electroactive (SEA) materials, mostly also referred to as dielectric elastomers (DEs) that can fast induce large deformation when subjected to an electric field, have emerged as an inspiring subject for their remarkable muscle-like capability (Bauer et al., 2014; Mirfakhrai et al., 2007; Mirvakili and Hunter, 2018; Suo, 2010; Zhang et al., 2002). Following the pioneering works of Pelrine et al. (1998), Pelrine et al. (2000), much effort has been devoted to the fabrication of optimized SEA materials and design of SEA-based devices (Bar-Cohen, 2004; Brochu and Pei, 2010; Carpi et al., 2008a; Mirvakili and Hunter, 2018; O'Halloran et al., 2008; Shankar et al., 2007; Trivedi et al., 2008). In these applications, the intricate electromechanical coupling effect and the strong nonlinearity due to large deformation in SEA materials usually lead to more complicated nonlinear responses than those of the pure elastic ones. To address the extra complexity from these two features, we may adopt the general nonlinear continuum theory of electroelasticity, which was first proposed by Toupin (1956) more than sixty years ago and has been given new impetus thanks to the explosive applications of SEA materials in the last two decades (Dorfmann and Ogden, 2010a, 2014; Suo et al., 2008). So far, such theory has been successfully implemented to solve various boundary-value problems of soft dielectrics, including instability, vibration, wave propagation, etc. (Dorfmann and Ogden, 2010b; Getz et al., 2017; Su et al., 2018; Wu et al., 2017). However, many fundamental questions on the behavior of SEA materials remain largely unanswered. In particular, more detailed and accurate microstructural information is still required for the design of SEA devices.

Nanoindentation and scanning probe microscopy (SPM) have been widely used to detect local material properties of membranes,

* Corresponding author.

https://doi.org/10.1016/j.ijsolstr.2020.09.035
0020-7683/

Nomenclature

List of main symbols

d	Indentation depth
a	Radius of contact
β	Half of the apex angle of a conical indenter
α_{1i}	Coefficients in displacement u_z, see Appendix A.2
σ_{z1}	Incremental normal stress
γ_{1i}	Coefficients in normal stress σ_{z1}, see Appendix A.2
$\sigma_{\rho 1}$	Incremental shear stress
K_1^{C}	Stress intensity factor for a conducting indenter, see Eq. (A26)
K_2^{C}	Electric displacement intensity factor, see Eq. (A26)
p_1^{C}	Total force on a conducting indenter, see Eq. (A44)
K_1^{I}	Stress intensity factor for an insulating indenter, see Eq. (A49)
p_1^{I}	Total force on an insulating indenter, see Eq. (A59)
$p_{\mathrm{ad}}^{\mathrm{I}}$	Pull-out force for an insulating flat-ended indenter, see Eq. (10)
$d_{\mathrm{cr}}^{\mathrm{I}}$	Displacement of an insulating flat-ended indenter when $p_1^{\mathrm{I}} = p_{\mathrm{ad}}^{\mathrm{I}}$, see Fig. 3 (a) and Eq. (11)
a_0	Radius of contact induced by adhesion, see Fig. 3 and Eqs. (12)–(16)
g_{jk}	$g_{jk} = \sum_{i=1}^{3} h_{ij}\alpha_{ki}, \quad (j,k = 1,2)$, effective material parameters in incremental stresses and electric displacements, see Appendix A.3
φ_0	Electric potential prescribed on a conducting indenter
η	Surface adhesion energy per unit area
R	Radius of a spherical indenter
α_{2i}	Coefficients in electric potential φ, see Appendix A.2
σ_{z2}	Incremental electric displacement
γ_{2i}	Coefficients in electric displacement σ_{z2}, see Appendix A.2
ϖ_{1i}	Coefficients in shear stress $\sigma_{\rho 1}$, see Appendix A.2
χ_1	Core function in the solution of σ_{z1} for a conducting indenter
χ_2	Core function in the solution of σ_{z2} for a conducting indenter
p_2^{C}	Total charge on a conducting indenter, see Eq. (A44)
χ_0	Core function in the solution of σ_{z1} for an insulating indenter
A_0	$A_0 = g_{11}g_{22} - g_{12}g_{21}$, defined in Appendix A.3
$p_{\mathrm{ad}}^{\mathrm{C}}$	Pull-out force for a conducting flat-ended indenter, see Eq. (10)
$d_{\mathrm{cr}}^{\mathrm{C}}$	Displacement of a conducting flat-ended indenter when $p_1^{\mathrm{C}} = p_{\mathrm{ad}}^{\mathrm{C}}$, see Fig. 3(a) and Eq. (11)
h_{ij}	Coefficients in potential function ψ_i, defined in Appendix B.1

biological materials, and other functional materials (Azzez et al., 2018; Bonilla et al., 2015; Choi et al., 2003; Ebenstein and Pruitt, 2006; Kolluru et al., 2018; Liu et al., 2012; Osmani et al., 2017; Racles et al., 2017; Saha and Nix, 2002; Zhang et al., 2014; Zhu et al., 2018; Zisis et al., 2015). These two techniques are well known for their high spatial resolution and easy manipulation. Furthermore, they are mechanically or electrically sensitive, without the need for large stimuli, and hence causing almost no damage to samples. These characteristics are of great importance in the characterization and test of SEA materials. It should be noted that the linear contact theory provides a general theoretical and technical guidance for these two approaches, despite their differences in technical details (Kalinin et al., 2007; Oliver and Pharr, 1992).

Ever since the original work initiated by Hertz (1881) for elasticity, the studies on contact problems have been generalized to piezoelectricity with electromechanical coupling. Giannakopoulos and Suresh (1999) developed a general theory for the axisymmetric indentation of piezoelectric materials by using Hankel transform and derived the relation between the indentation force and the depth of penetration. Chen and his co-workers (Chen, 2000; Chen and Ding, 1999; Chen et al., 1999) presented a series of complete and exact solutions for the normal contact between three typical axisymmetric punches (flat-ended, conical, and spherical) and a transversely isotropic piezoelectric half-space by using the potential theory method originally proposed by Fabrikant (1989), Fabrikant (1991). Their results were later verified by Kalinin and his partners (Kalinin et al., 2004; Karapetian et al., 2005), who first related the SPM responses to the three-dimensional (3D) analytical expressions for the generalized Hertz contact model. Through their persistent efforts, the importance of exact 3D contact solutions is now widely understood for a more quantitative interpretation of the SPM responses (Kalinin et al., 2007; Karapetian et al., 2009). For example, these 3D solutions may serve as a theoretical foundation for the reconstruction of 3D physical properties of the sample with a single scan on its surface by the SPM probe. It causes almost no damage to the sample when compared with a newly developed conductive tomographic atomic force microscopy (Luria et al., 2016). It should be noted that the SPM discussed here works under contact mode, which should be clearly distinguished from that working under non-contact mode (Li et al., 2015). The latter relies on the dynamic resonance of the probe-sample system. The detailed descriptions of these two modes can be found in the two most recent papers of Pan et al. (2013) and Zhu et al. (2018).

It is well known that pre-stretching SEA materials may enhance their electromechanical properties dramatically (Akbari et al., 2013; Arora et al., 2007; Brochu and Pei, 2010; Carpi and De Rossi, 2004; Kofod et al., 2003; Li et al., 2019; Linnebach et al., 2019; Löwe et al., 2005; McKay et al., 2011; Rizzello et al., 2016; Shian et al., 2013; Su et al., 2019; Suo, 2012). Contact analysis of a finitely deformed elastomer was first conducted by Green et al. (1952), who considered the typical problem of a pre-strained incompressible isotropic semi-infinite region pressed by a smooth punch based on the general theory of small elastic deformations superposed on finite elastic deformations. Beatty and Usmani (1975) extended the analysis to compressible isotropic materials and a detailed discussion was presented on the relation between indentation response and load. These earlier results have been taken as benchmark solutions when the electromechanical coupling is absent. For example, Zheng et al. (2017) recently used the surface Green's function to investigate the effect of pre-stretch on the indentation response of elastomers. Their results perfectly agree with Beatty and Usamni's work when considering an equi-biaxially stretched elastomer. However, they only focused on the purely elastic problems so that their results are not applicable to the electromechanical indentation analysis of SEA materials. Moreover, they did not consider the effect of adhesion, which may play a significant role in the contact responses of soft elastomers. It should be noted that, there are basically two strategies to probe the material properties of soft materials. One is to derive approximate analytical contact relations directly based on the nonlinear continuum theory (Dagro and Ramesh, 2019), but a corresponding nonlinear indentation technique is also required. In this paper, following the strategy initiated by Green et al. (1952), we will employ the full nonlinear continuum theory in the pre-deformation state, but restrict the contact deformation to be infinitesimally small. In this case, we can use a uniform

pre-deformation (may be finite) to stiffen the soft material, and then use the linear contact theory for probing the material properties for which all technique details are already there or can be readily improved. In this regard, the latter strategy, though a little counterintuitive, may be practically more feasible and economic.

Recently, Zhang et al. (2012) conducted an indentation analysis of a compressible isotropic SEA half-space subjected to a uniform finite deformation. It is the only theoretical work on contact problem concerning the concurrent effects of finite pre-deformation and electromechanical coupling of SEA materials, to our best knowledge. In their analysis, in addition to a uniform finite equi-biaxial pre-stretch in the planes parallel to the free surface, a uniform electric displacement is further applied which is perpendicular to the plane surface. It is found that the governing equations of the incremental fields are similar to those of a transversely isotropic piezoelectric body. Thus, the potential theory developed by Fabrikant (1989), Fabrikant (1991) for elasticity and its extension in piezoelectricity (Chen, 2000, 2015; Chen and Ding, 1999, 2004; Chen et al., 1999) can easily be extended to deal with the contact problem of an SEA half-space indented by three typical axisymmetric indenters. The results in Zhang et al. (2012) are mathematically beautiful and complete, but there is also no account of the effect of adhesion, which however has frequently proved to be indispensable in the tests of soft materials at nanoscale (Cao et al., 2005; Ebenstein and Pruitt, 2006; Gupta et al., 2007; Schwarz, 2003; Zisis et al., 2011). Therefore, it becomes necessary and also interesting to carry out adhesive contact analysis for SEA materials.

There are three prevailing theories or models in adhesive contact analysis, i.e. the JKR model (Johnson et al., 1971), the DMT model (Derjaguin et al., 1975), and the MD model (Maugis, 1992). The core ideas of these theories have been successfully transplanted into the indentation analysis of piezoelectric materials (Chen, 2009; Chen and Yu, 2005; Yang, 2006). Thus, they may be further utilized without essential mathematical difficulty to account for the adhesion effect during the indentation of the above mentioned uniformly deformed SEA half-space. In this paper, a modified JKR model (Lu et al., 2011; Maugis, 2000) is employed to study the effect of adhesion by taking into account the change of surface adhesion energy during the contact. We obtain a series of exact solutions for the 3D electroelastic field in the half-space. Most interestingly, for a depth-fixed, non-adhesive indentation test of the SEA half-space, we observe that, as the biasing electric displacement reaches a critical value, the incremental normal stress may vanish and even become tensile. We demonstrate that this abnormal phenomenon is caused by the surface instability of the elastomer, which is similar to that in the purely elastic case studied by Beatty and Usmani (1975). Further, when considering the role of adhesion on indentation responses, we find that, by taking spherical indentation as an example, the ratio of contact radius to the radius of indenter increases with the increasing electric biasing field, and the incremental normal strain induced by indention can exceed the regime of small (infinitesimal) deformation before the onset of surface instability. Hence, the indentation analysis based on the linear elastic theory becomes invalid for SEA materials prior to instability. That is, the indentation-induced linear (incremental) deformation is limited by the geometry of the indenter (e.g. the radius of a spherical indenter), indentation depth as well as the magnitude of the surface adhesion energy. These findings imply two essential rules for the depth-fixed indentation test of SEA materials with surface adhesion: (1) Measurements on a pre-stressed SEA sample may fail due to the surface instability induced by the electric biasing field; (2) When the sample is subjected to a sufficiently large electric biasing field but without loss of stability, effective measurements can only be realized by properly reducing the surface adhesion energy and/or minishing the indentation depth without sacrificing the resolution of indentation image (i.e. increasing the indenter size).

The paper is structured as follows. In Section 2, we give the basic equations governing an SEA half-space subject to a uniform equi-biaxial stretch and a unidirectional electric displacement. In Section 3, the exact 3D adhesive contact solutions for three typical axisymmetric indenters (flat-ended, conical, and spherical) are presented in terms of elementary functions, with the main analytical results summarized in Tables 2 and 3. For illustration, numerical examples are considered for a compressible neo-Hookean SEA half-space in Section 4. The present exact solutions are validated by comparing with the finite element (FE) simulations in the degenerated case of an elastic half-space. For the surface instability of the SEA half-space, a certain difference in the curves of critical electric displacement versus pre-stretch is observed between the electrically conducting surface conditions and the electrically insulating ones. Moreover, we carefully discuss the validity of the indentation analysis under the framework of linear elasticity for the incremental deformation. Finally, the electroelastic field variables on the surface of the half-space under spherical and conical indenters in adhesive and non-adhesive contact cases are given and compared, which directly indicate the significant influences of adhesion and electric biasing field. We summarize our conclusions in the last section.

2. Governing equations of a uniformly pre-deformed SEA body

We consider the contact between a rigid indenter and a pre-deformed SEA half-space, which is subject to a uniform equi-biaxial stretch λ_1 in the $x_1 - x_2$ plane and a uniform stretch λ_3 in the direction perpendicular to the surface $x_3 = 0$ as shown in Fig. 1. The half-space is simultaneously under an electric displacement vector $\boldsymbol{D}$ (in Euler form) with the non-zero component only in the x_3 direction. Dorfmann and Ogden (2010b) developed an excellent general framework to describe the nonlinear electroelastic response of SEA materials. The linearized equations governing the infinitesimal incremental motion superimposed on a finitely deformed SEA body were also established (Dorfmann and Ogden, 2010b). All the essential formulations are summarized in Appendix A.1.

The pre-deformed state of the SEA half-space then can be

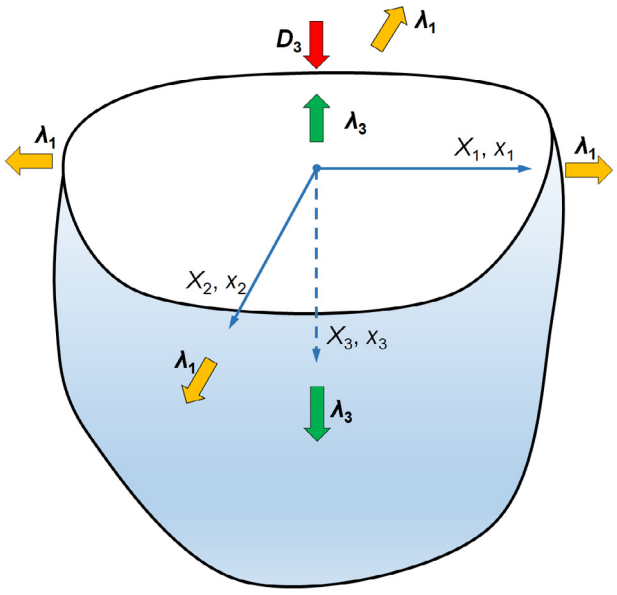

Fig. 1. The uniformly pre-deformed half-space and the Cartesian coordinates.

described by

$$\boldsymbol{F}=\mathrm{diag}(\lambda_1,\lambda_1,\lambda_3),\ \boldsymbol{b}=\boldsymbol{c}=\mathrm{diag}(\lambda_1^2,\lambda_1^2,\lambda_3^2),\ \boldsymbol{D}=[0,0,D_3]^{\mathrm{T}} \tag{1}$$

where $\boldsymbol{F}$ is the deformation gradient tensor, and $\boldsymbol{b}$ and $\boldsymbol{c}$ are the left and right Cauchy-Green tensors, respectively. For the incremental field superimposed on the above pre-deformed state of an isotropic SEA half-space, the following linear constitutive equations can be obtained (Dorfmann and Ogden, 2010b)

$$\begin{aligned}
&\dot{T}_{011}=c_{11}\tfrac{\partial u_1}{\partial x_1}+c_{12}\tfrac{\partial u_2}{\partial x_2}+c_{13}\tfrac{\partial u_3}{\partial x_3}+e_{31}\tfrac{\partial \varphi}{\partial x_3},\\
&\dot{T}_{022}=c_{12}\tfrac{\partial u_1}{\partial x_1}+c_{11}\tfrac{\partial u_2}{\partial x_2}+c_{13}\tfrac{\partial u_3}{\partial x_3}+e_{31}\tfrac{\partial \varphi}{\partial x_3},\\
&\dot{T}_{033}=c_{13}\tfrac{\partial u_1}{\partial x_1}+c_{13}\tfrac{\partial u_2}{\partial x_2}+c_{33}\tfrac{\partial u_3}{\partial x_3}+e_{33}\tfrac{\partial \varphi}{\partial x_3},\\
&\dot{T}_{012}=c_{69}\tfrac{\partial u_1}{\partial x_2}+c_{66}\tfrac{\partial u_2}{\partial x_1},\ \dot{T}_{031}=c_{88}\tfrac{\partial u_1}{\partial x_3}+c_{58}\tfrac{\partial u_3}{\partial x_1}+e_{15}\tfrac{\partial \varphi}{\partial x_1},\\
&\dot{T}_{021}=c_{66}\tfrac{\partial u_1}{\partial x_2}+c_{69}\tfrac{\partial u_2}{\partial x_1},\ \dot{T}_{023}=c_{58}\tfrac{\partial u_2}{\partial x_3}+c_{55}\tfrac{\partial u_3}{\partial x_2}+e_{15}\tfrac{\partial \varphi}{\partial x_2},\\
&\dot{T}_{013}=c_{58}\tfrac{\partial u_1}{\partial x_3}+c_{55}\tfrac{\partial u_3}{\partial x_1}+e_{15}\tfrac{\partial \varphi}{\partial x_1},\ \dot{T}_{032}=c_{88}\tfrac{\partial u_2}{\partial x_3}+c_{58}\tfrac{\partial u_3}{\partial x_2}+e_{15}\tfrac{\partial \varphi}{\partial x_2},
\end{aligned} \tag{2}$$

$$\begin{aligned}
&\dot{D}_{l01}=e_{15}\left(\tfrac{\partial u_1}{\partial x_3}+\tfrac{\partial u_3}{\partial x_1}\right)-\varepsilon_{11}\tfrac{\partial \varphi}{\partial x_1},\\
&\dot{D}_{l02}=e_{15}\left(\tfrac{\partial u_2}{\partial x_3}+\tfrac{\partial u_3}{\partial x_2}\right)-\varepsilon_{11}\tfrac{\partial \varphi}{\partial x_2},\\
&\dot{D}_{l03}=e_{31}\left(\tfrac{\partial u_1}{\partial x_1}+\tfrac{\partial u_2}{\partial x_2}\right)+e_{33}\tfrac{\partial u_3}{\partial x_3}-\varepsilon_{33}\tfrac{\partial \varphi}{\partial x_3},
\end{aligned} \tag{3}$$

where u_i are the components of the incremental displacement vector, φ is the electric potential, $\dot{T}_{0ij}$ are the components of the "push-forward" incremental nominal stress tensor, and $\dot{D}_{l0i}$ are the components of the "push-forward" incremental Lagrangian electric displacement vector. c_{ij}, e_{ij}, and ε_{ij} are the effective elastic, piezoelectric and dielectric constants, which depend on the pre-deformation. In the current situation, these constants are functions of λ_1, λ_3 and D_3.

The equilibrium equations for the incremental field are provided in Eq. (A5), where the last equation is automatically satisfied by noticing that the "push-forward" incremental Lagrangian electric field vector is expressed as the negative gradient of the electric potential (i.e. $\dot{\boldsymbol{E}}_{l0}=-\mathrm{grad}\varphi$). According to Zhang et al. (2012), the general solution to the governing equations in Eqs. (2), (3) and (A5) for axisymmetric problems in cylindrical coordinates (ρ,θ,z) is

$$\begin{aligned}
&u_\theta=0,\ w_1\equiv u_z=\sum_{i=1}^{3}\alpha_{1i}\tfrac{\partial \psi_i}{\partial z_i},\\
&u_\rho=\sum_{i=1}^{3}\tfrac{\partial \psi_i}{\partial \rho},\ w_2\equiv\varphi=\sum_{i=1}^{3}\alpha_{2i}\tfrac{\partial \psi_i}{\partial z_i},
\end{aligned} \tag{4}$$

where ψ_i $(i=1,\ 2,\ 3)$ are quasi-harmonic functions satisfying Eq. (A10), ρ is the radial coordinate, and $z_i=s_iz=s_ix_3$, with s_i and α_{2i} all defined in Appendix A.2. The incremental stresses and electric displacements can be obtained accordingly as

$$\begin{aligned}
&\sigma_{z1}\equiv\dot{T}_{0zz}=\sum_{i=1}^{3}\gamma_{1i}\tfrac{\partial^2\psi_i}{\partial z_i^2},\quad \sigma_{\rho1}\equiv\dot{T}_{0z\rho}=\sum_{i=1}^{3}\varpi_{1i}\tfrac{\partial^2\psi_i}{\partial\rho\partial z_i},\\
&\sigma_{z2}\equiv\dot{D}_{l0z}=\sum_{i=1}^{3}\gamma_{2i}\tfrac{\partial^2\psi_i}{\partial z_i^2},\quad \sigma_{\rho2}\equiv\dot{T}_{0\rho z}=\sum_{i=1}^{3}\varpi_{2i}\tfrac{\partial^2\psi_i}{\partial\rho\partial z_i},\\
&\sigma_{z3}\equiv\dot{T}_{0\rho\rho}+\dot{T}_{0\theta\theta}=\sum_{i=1}^{3}\gamma_{3i}\tfrac{\partial^2\psi_i}{\partial z_i^2},\quad \sigma_{\rho3}\equiv\dot{D}_{l0\rho}=\sum_{i=1}^{3}\varpi_{3i}\tfrac{\partial^2\psi_i}{\partial\rho\partial z_i}.
\end{aligned} \tag{5}$$

where γ_{ij} and ϖ_{ij} are also defined in Appendix A.2.

3. Exact adhesive contact analysis

3.1. Indentation by a rigid punch

The adhesive contact of a pre-deformed compressible SEA half-space with an axisymmetric rigid indenter is depicted in Fig. 2. The shape of the indenter is assumed to be described by a general power series

$$f(\rho)=\sum_{n=1}^{\infty}r_n\rho^n, \tag{6}$$

where r_n $(n=1,2,\ldots)$ are the shape parameters. For the three common indenters (i.e. flat-ended, conical, and spherical), these parameters are explicitly listed in Table 1, where β and R are the half of the apex angle of the cone and the radius of the spherical indenter, respectively, and δ_{nk} is the Kronecker delta.

The contact is assumed to be perfectly frictionless. The mechanical boundary conditions are therefore given as

$$\begin{cases}
0\leqslant\rho\leqslant a, & u_z=d-f(\rho),\\
\rho>a, & \sigma_{z1}=0,\\
\rho\geqslant 0, & \sigma_{\rho1}=0,
\end{cases} \tag{7}$$

while the electrical boundary conditions are

$$\begin{cases}
0\leqslant\rho\leqslant a, & \varphi=\varphi_0,\\
\rho>a, & \sigma_{z2}=0,
\end{cases} \tag{8}$$

for perfectly conducting indenters, and

$$\rho\geqslant 0, \qquad \sigma_{z2}=0, \tag{9}$$

for perfectly insulating indenters. As indicated in Fig. 2, a and d are the contact radius and indentation depth respectively.

We can utilize the generalized potential theory method (Chen, 2000; Chen and Ding, 1999; Chen et al., 1999) to solve the above contact problem. A prominent feature is that we here apply the modified JKR model to take account of the adhesive effect during indentation. The full details of derivation are provided in Appendices A.3 (for the conducting case) and A.4 (for the insulating case).

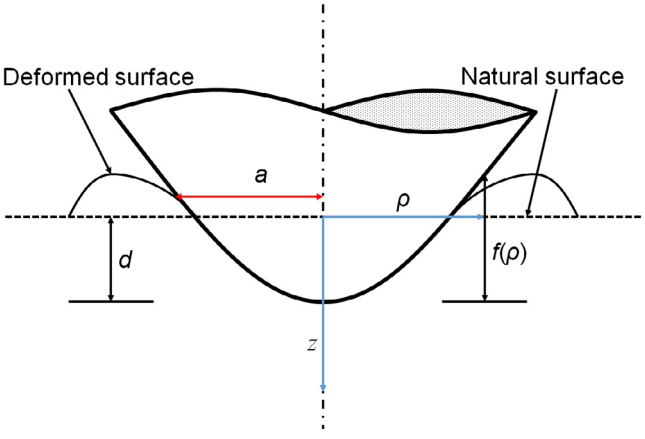

Fig. 2. An axisymmetric rigid indenter pressed into an elastic half-space.

Table 1
Shape parameters for three common indenters.

Quantity	Flat-ended	Conical	Spherical
r_n	0	$\delta_{n1}\cot\beta$	$\delta_{n2}(2R)^{-1}$

Table 2
Analytical contact relations for three axisymmetric conducting indenters.

Quantity	Flat-ended	Conical	Spherical
$\chi_1(t)$	$(g_{22}d-g_{21}\varphi_0)/A_0$	$g_{22}(d-\pi t\cot\beta/2-g_{21}\varphi_0/g_{22})/A_0$	$g_{22}(d-t^2/R-g_{21}\varphi_0/g_{22})/A_0$
$\sigma_{z1}(\rho)$	$\frac{g_{22}d-g_{21}\varphi_0}{\pi^2A_0\sqrt{a^2-\rho^2}}$	$\frac{\sqrt{a/\pi}K_1^C}{\sqrt{a^2-\rho^2}}+\frac{g_{22}\cot\beta\cosh^{-1}(a/\rho)}{2\pi A_0}$	$\frac{\sqrt{a/\pi}K_1^C}{\sqrt{a^2-\rho^2}}+\frac{2\sqrt{a^2-\rho^2}}{g_{22}^{-1}\pi^2RA_0}$
$p_1^C(a,d)$	$\frac{2a(g_{21}\varphi_0-g_{22}d)}{\pi A_0}$	$\frac{2a(\varphi_0g_{21}-g_{22}d)}{\pi A_0}+\frac{a^2\cot\beta}{2g_{22}^{-1}A_0}$	$\frac{2a(\varphi_0g_{21}-g_{22}d)}{\pi A_0}+\frac{2a^3g_{22}}{3\pi A_0R}$
$p_1^C(a,\eta)$	—	$\frac{a\varphi_0}{\pi g_{21}^{-1}A_0}-\frac{g_{22}a^2\cot\beta}{2A_0}$ $-2a\sqrt{(\frac{g_{21}\varphi_0}{2\pi A_0})^2-\frac{2aA_0^{-1}g_{22}\eta}{(1+\cot^2\beta)^{-1/2}}}$	$\frac{a\varphi_0}{\pi g_{21}^{-1}A_0}-\frac{4g_{22}a^3}{3\pi A_0R}$ $-2a\sqrt{(\frac{g_{21}\varphi_0}{2\pi A_0})^2-\frac{2aA_0^{-1}g_{22}\eta}{(1+a^2/R^2)^{-1/2}}}$
$d(a,p_1^C)$	$\frac{\pi A_0p_1^C}{-2ag_{22}}+\frac{\varphi_0g_{21}}{g_{22}}$	$\frac{\pi A_0p_1^C}{-2ag_{22}}+\frac{\varphi_0g_{21}}{g_{22}}+\frac{\pi a\cot\beta}{4}$	$\frac{\pi A_0p_1^C}{-2ag_{22}}+\frac{\varphi_0g_{21}}{g_{22}}+\frac{a^2}{3R}$
$d(a,\eta)$	—	$\frac{g_{21}\varphi_0}{2g_{22}}+\frac{\pi a\cot\beta}{2}$ $+\frac{\sqrt{(g_{21}\varphi_0)^2-8a\pi^2A_0g_{22}\eta\sqrt{1+\cot^2\beta}}}{2g_{22}}$	$\frac{g_{21}\varphi_0}{2g_{22}}+\frac{a^2}{R}$ $+\frac{\sqrt{(g_{21}\varphi_0)^2-8a\pi^2A_0g_{22}\eta\sqrt{1+a^2/R^2}}}{2g_{22}}$
$\chi_2(t)$	$\frac{g_{11}\varphi_0-g_{12}d}{A_0}$	$\frac{-g_{12}}{A_0}\left(d-\frac{\pi t\cot\beta}{2}-\frac{g_{11}}{g_{12}}\varphi_0\right)$	$\frac{-g_{12}}{A_0}\left(d-\frac{t^2}{R}-\frac{g_{11}}{g_{12}}\varphi_0\right)$
$\sigma_{z2}(\rho)$	$\frac{g_{11}\varphi_0-g_{12}d}{\pi^2A_0\sqrt{a^2-\rho^2}}$	$\frac{\sqrt{a/\pi}K_2^C}{\sqrt{a^2-\rho^2}}+-\frac{g_{12}\cot\beta\cosh^{-1}(a/\rho)}{2\pi A_0}$	$\frac{\sqrt{a/\pi}K_2^C}{\sqrt{a^2-\rho^2}}+-\frac{2\sqrt{a^2-\rho^2}}{g_{12}^{-1}\pi^2RA_0}$
$p_2^C(a,d)$	$\frac{2a(g_{12}d-g_{11}\varphi_0)}{\pi A_0}$	$\frac{2a(g_{12}d-g_{11}\varphi_0)}{\pi A_0}-\frac{a^2\cot\beta}{2g_{12}^{-1}A_0}$	$\frac{2a(g_{12}d-g_{11}\varphi_0)}{\pi A_0}-\frac{2a^3R^{-1}}{3\pi g_{12}^{-1}A_0}$
$p_2^C(a,\eta)$	—	$\frac{g_{12}}{2A_0}a^2\cot\beta-\frac{(2g_{11}g_{22}-g_{12}g_{21})a\varphi_0}{\pi A_0g_{22}}$ $+\frac{\sqrt{(g_{21}\varphi_0)^2-8a\pi^2A_0g_{22}\eta\sqrt{1+\cot^2\beta}}}{\pi g_{12}^{-1}g_{22}A_0a^{-1}}$	$\frac{4g_{12}a^3}{3\pi A_0R}-\frac{(2g_{11}g_{22}-g_{12}g_{21})a\varphi_0}{\pi A_0g_{22}}$ $+\frac{\sqrt{(g_{21}\varphi_0)^2-8a\pi^2A_0g_{22}\eta\sqrt{1+a^2/R^2}}}{\pi g_{12}^{-1}g_{22}A_0a^{-1}}$

3.2. Adhesive contact of three typical indenters

For three common circular rigid indenters (flat-ended, spherical and conical), specific results can be obtained by substituting the corresponding profile functions into Eqs. (A28), (A38)–(A41), (A50), and (A54)–(A56). These analytical results are summarized in Tables 2 and 3 for conducting and insulating indenters respectively. It is noted that when the adhesive effect is removed, the results of Zhang et al. (2012) will be recovered. In the text to follow, we will use the results in Tables 2 and 3 to discuss some particular indentation behaviors during the adhesive contact between the three typical indenters and the pre-deformed soft electroactive half-space.

3.2.1. Flat-ended circular punch

For a circular flat-ended punch, the contact relations shown in the first column of Table 2 or 3 are adhesion-independent. The effect of adherence force only emerges during the separation of the probe-sample system as shown in Fig. 3(a). Following Maugis (2000) but omitting details, we express the adherence force as

$$|p_{ad}^{I}|=2a\sqrt{-\frac{2a}{g_{11}}\eta},$$

$$|p_{ad}^{C}|=\frac{a}{A_0\pi}\left[\sqrt{(g_{21}\varphi_0)^2-8a\pi^2A_0g_{22}\eta}-g_{21}\varphi_0\right], \tag{10}$$

which are the minimal tensile forces (also called as pull-out forces) to completely detach the punch from the surface of the sample at the respective critical displacements

$$d_{cr}^{I}=\sqrt{-2a\pi^2g_{11}\eta},$$

$$d_{cr}^{C}=(2g_{22})^{-1}\left[\sqrt{(g_{21}\varphi_0)^2-8a\pi^2A_0g_{22}\eta}+g_{21}\varphi_0\right]. \tag{11}$$

3.2.2. Conical punch

For a conical punch as shown in Fig. 3(b), according to Eqs. (A45) and (A60), we get the radius of contact induced by adhesion as

Table 3
Analytical contact relations for three axisymmetric insulating indenters.

Quantity	Flat-ended	Conical	Spherical
$\chi_0(t)$	$\frac{d}{g_{11}}$	$\frac{1}{g_{11}}\left(d-\frac{\pi t\cot\beta}{2}\right)$	$\frac{1}{g_{11}}\left(d-\frac{t^2}{R}\right)$
σ_{z1}	$\frac{\pi^{-2}g_{11}^{-1}d}{\sqrt{a^2-\rho^2}}$	$\frac{\sqrt{\frac{a}{\pi}}K_1^I}{\sqrt{a^2-\rho^2}}+\frac{\cot\beta\cosh^{-1}(\frac{a}{\rho})}{2\pi g_{11}}$	$\frac{\sqrt{\frac{a}{\pi}}K_1^I}{\sqrt{a^2-\rho^2}}+\frac{2\sqrt{a^2-\rho^2}}{g_{11}\pi^2R}$
$p_1^I(a,d)$	$-\frac{2ad}{\pi g_{11}}$	$-\frac{2ad}{\pi g_{11}}+\frac{a^2\cot\beta}{2g_{11}}$	$-\frac{2ad}{\pi g_{11}}+\frac{2a^3R^{-1}}{3\pi g_{11}}$
$p_1^I(a,\eta)$	—	$\frac{-a^2\cot\beta}{2g_{11}}-2a\sqrt{-\frac{2a}{g_{11}}\eta\sqrt{1+\cot^2\beta}}$	$\frac{-4a^3}{3\pi g_{11}R}-2a\sqrt{-\frac{2a}{g_{11}}\eta\sqrt{1+a^2/R^2}}$
$d(a,p_1^I)$	$\frac{\pi g_{11}}{-2a}p_1^I$	$\frac{\pi g_{11}}{-2a}p_1^I+\frac{\pi a\cot\beta}{4}$	$\frac{\pi g_{11}}{-2a}p_1^I+\frac{a^2}{3R}$
$d(a,\eta)$	—	$\frac{\pi a\cot\beta}{2}-\pi\sqrt{-2ag_{11}\eta\sqrt{1+\cot^2\beta}}$	$\frac{a^2}{R}-\pi\sqrt{-2ag_{11}\eta\sqrt{1+a^2/R^2}}$

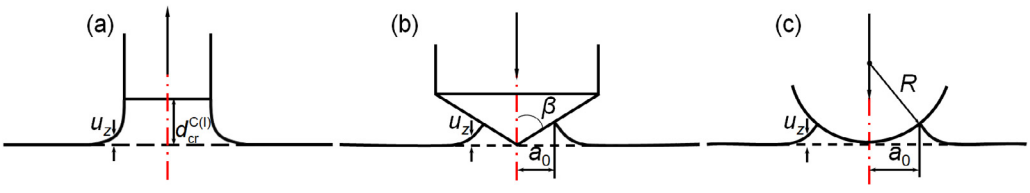

Fig. 3. The adherence of three common axisymmetric indenters: (a) flat-ended; (b) conical; (c) spherical.

$$a_0 = -\frac{32g_{11}\eta\sqrt{1+\cot^2\beta}}{\cot^2\beta}, \tag{12}$$

for the insulating case, and

$$a_0 = -\frac{32A_0\eta\sqrt{1+\cot^2\beta}}{g_{22}\cot^2\beta} + \frac{4g_{21}\varphi_0}{\pi g_{22}\cot\beta}, \tag{13}$$

for the conducting case.

3.2.3. Spherical punch

For a spherical punch as shown in Fig. 3(c), according to Eqs. (A45) and (A60), we get the radius of contact induced by adhesion as

$$a_0^6 - \frac{y_0^2}{R^2}a_0^2 - y_0^2 = 0, \tag{14}$$

for the insulating case, and

$$a_0^6 - 2y_2a_0^4 + \left(y_2^2 - \frac{y_1^2}{R^2}\right)a_0^2 - y_1^2 = 0, \tag{15}$$

for the conducting case, where

$$y_0 = -\frac{9\pi^2R^2g_{11}\eta}{2},\ y_1 = -\frac{9\pi^2R^2A_0\eta}{2g_{22}},\ y_2 = \frac{3g_{21}R\varphi_0}{2g_{22}}. \tag{16}$$

4. Numerical results and discussion

The exact electroelastic fields in the half-space can be obtained for specific indenters, and the explicit results are given in Appendix C. For illustration, we present several numerical examples in this section. We first check our theoretical solutions in Section 4.1 through comparison with FE simulations in the purely elastic case. Section 4.2 considers the indentation response of a neo-Hookean electroactive half-space by a flat-ended punch as well as its relation to surface instability of the half-space due to pre-deformation when a particular phenomenon occurs. The mathematical details of the stability analysis are however given in Appendix D. Then we highlight the validity of the linear exact solutions for the indentation test in Section 4.3 by taking spherical indentation as an example. The influences of adhesion and the modification of contact area on the indentation responses for spherical and conical indenters are studied in Section 4.4. Note that the traction-free condition is always assumed during all indentation analysis while the values of shape parameters of the indenters are essentially chosen according to the common tip size of SPM probes (Calabri et al., 2008; Li et al., 2008; Pan et al., 2013).

4.1. Verification of the exact solutions

We consider a degenerated model, i.e. the indentation of a compressible neo-Hookean elastic half-space by a circular flat-ended rigid indenter. The initial shear modulus and Poisson's ratio are set to be 1 MPa and 0.3, respectively. In this case, all the analytical results keep unchanged except that the electric field and the electromechanical coupling should be discarded (Chen et al., 2010). The commercial finite element software ABAQUS 2016 is employed for the purpose of verification. The numerical model comprises of a total of 11,907 four-node bilinear axisymmetric reduced integration elements and 12,037 nodes. A denser mesh is designed at or near the contact region, as shown in Fig. 4(a). We set $\lambda_1 = \lambda_2 = 1.05$ and λ_3 is determined from the traction-free surface condition. Also, we denote the total load acting on the punch as p_0, which induces an indentation depth (d). Fig. 4(b) and (c) and 6 display the distributions of the vertical and radial displacements (normalized by d) at different vertical positions (or depths, normalized by a, the radius of the punch), and the comparison between the theoretical and numerical results indicates a good agreement, which validates the present mathematical derivations.

4.2. Indentation response of a neo-Hookean electroactive half-space by a flat-ended punch

Now, consider an electroactive half-space governed by the following neo-Hookean type of energy density function (Huang et al., 2016)

$$\Omega(\boldsymbol{F}, \boldsymbol{D}_l) = \frac{\mu}{2\kappa}(J^{-2\kappa} - 1) + \frac{\mu}{2}(I_1 - 3) + \frac{1}{J\varepsilon_0}(\zeta_1 I_4 + \zeta_2 I_5), \tag{17}$$

where $\kappa = \nu/(1-2\nu)$, the constants μ, ν and $\varepsilon_0 = 8.854 \times 10^{-12}$F/m are the initial shear modulus, Poisson's ratio and dielectric permittivity in vacuum, respectively, and ζ_1 and ζ_2 are two dimensionless electromechanical coupling coefficients. For the special case of $\zeta_1 = 0$ and $2\zeta_2 = \varepsilon^{-1}$, this model reduces to that of the so-called ideal dielectric elastomer (Zhao and Suo, 2007), where ε is the relative permittivity of the material. We take $\mu = 1.5$ MPa in the following calculations if necessary. Also, a dimensionless measure of D_3 is introduced as $\delta = D_3/\sqrt{\mu\varepsilon_0}$.

First of all, we consider a perfectly conducting and grounded ($\varphi_0 = 0$) circular flat-ended punch indenting an equi-biaxially pre-stretched SEA half-space with $\nu = 0.3$ and $\varepsilon = 1$. As in the last subsection, we have $\lambda_1 = \lambda_2 = \lambda$ (but its value can be varied) and $\lambda_3 = \chi$ is determined according to the traction-free surface condition. Recall that the surface adhesion energy does not play a role during the indentation by a flat-ended punch. Fig. 5 displays the variation of the incremental normal stress (σ_{z1}) at the center of the contact region with the biasing electric displacement (δ) for varying pre-stretches (λ = 0.55, 1, 1.45 and 1.9). Here the contact radius and indentation depth are fixed as 25 nm and 0.1 nm, respectively. For $\lambda = 0.55$ and $\delta = 0$, the problem reduces to the case of purely elastic compression. We can see that tensile normal stress occurs at the center of the contact region, which is quite abnormal. This unusual response is actually caused by surface instability of the half-space. The study on this topic can be traced back to the works of Green and Zerna (1954), Nowinski (1969), and Usmani and Beatty (1974). Beatty and Usmani (1975) pointed out that the surface instability could be accurately described by the vanishing of the normal indentation force and there is no surface instability of an elastic neo-Hookean half-space when it is under a state of biaxial tension ($\lambda > 1$). For the other three pre-deformed states (i.e. λ = 1, 1.45 and 1.9), the originally compressive stress for $\delta = 0$ also becomes tensile once the biasing electric displacement exceeds a critical value. It is clear that the tensile pre-stretch should not be responsible for this abnormity as noticed by Beatty and Usmani (1975). It becomes even clearer that the abnormal variation of stress still shows up when no equi-biaxial mechanical pre-stretch is applied in the case of $\lambda = 1$. Thus, the appearance of tensile stress as indicated in Fig. 5 for λ = 1, 1.45 and 1.9 should be due to the surface instability of the half-space induced by the increasing applied electric biasing field.

Now we consider the effects of the biasing electric displacement on the surface instability of the half-space, with the results presented in Fig. 6, which shows the variations with the electric displacement δ of the critical values of the in-plane pre-stretch (λ_{cr}), the vertical pre-stretch (χ_{cr}) and the critical volume ratio (J_{cr}). The points in the region above the solid curve of λ_{cr} correspond to compressive stresses while those below will induce tensile stresses. Note that the vanishing of incremental normal stress at the center of contact region is equivalent to the vanishing of indentation force, both corresponding to $g_{22} = 0$ (see the related formulae in Table 2). It is seen that the $\lambda_{cr} - \delta$ curve exhibits a particular

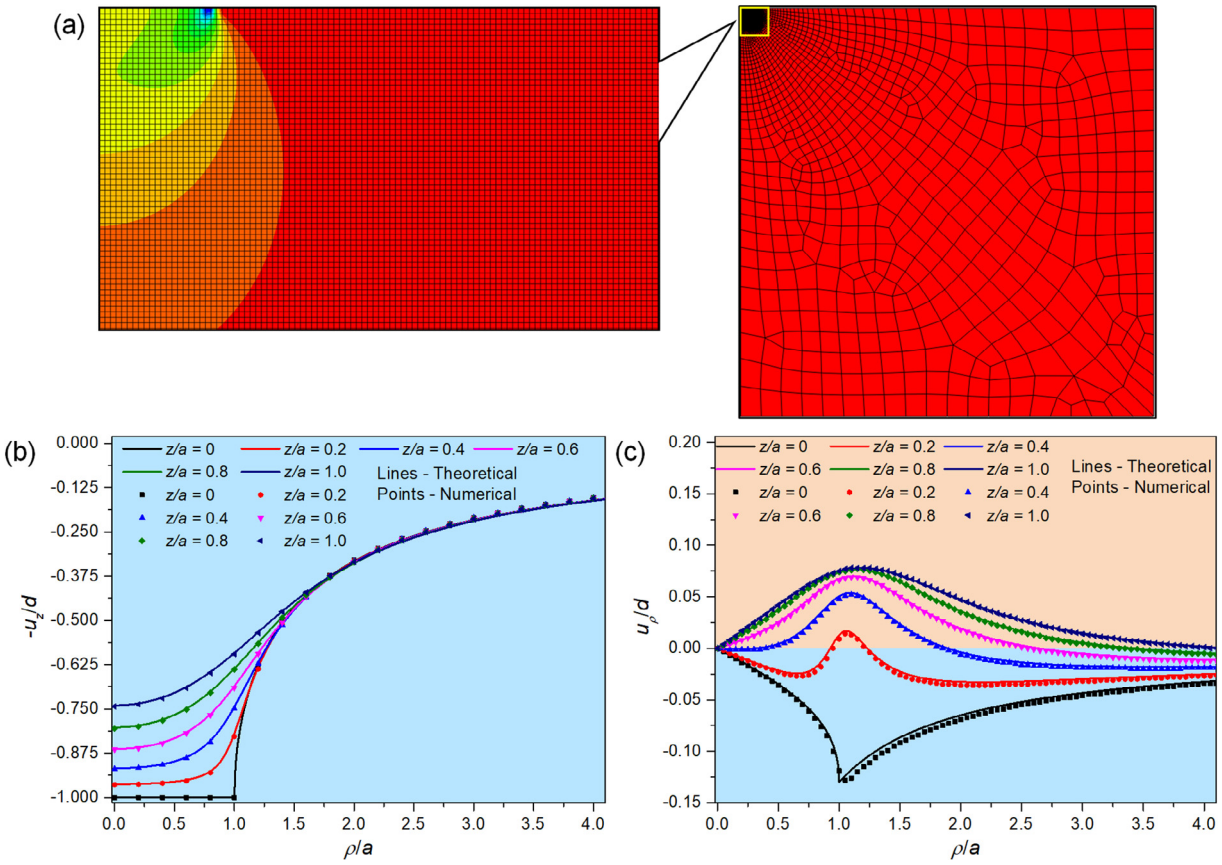

Fig. 4. Comparison of incremental displacement field obtained by numerical simulation and exact solutions of flat punch indentation: (a) finite element model in ABAQUS 2016; plots of (b) $-u_z/d$ and (c) u_ρ/d versus ρ/a at diverse depths respectively.

nonlinear character – it keeps rising slowly at the beginning, then goes up sharply, and finally slows down again. The influence of the electric property of the punch on the critical stretch under different biasing electric displacements can be checked by comparing Figs. 5 and 6 with Figs. E1 and E2 in Appendix E, the latter two presenting the parallel results in the case of a perfectly insulating indenter.

We demonstrate in Fig. 7 more explicitly, through the $\delta_{cr} - \lambda$ curve, the correlation between the abnormal phenomenon of the appearance of tensile contact stress during the indentation (Fig. 5) and the surface instability (Fig. 6) of the SEA half-space. We can see that the curve for the conducting (or insulating) indenter obtained according to the appearance of tensile contact stress perfectly matches that predicted by the instability analysis of the half-space with prescribed surface electric potential (or surface free charge). Thus, it confirms that the abnormal phenomenon of tensile incremental normal stress in Fig. 5 is due to the loss of sta-

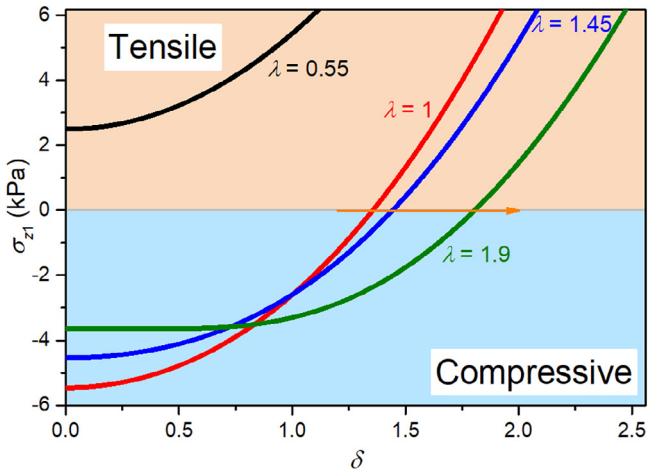

Fig. 5. Plot of the incremental normal stress (σ_{z1}) at the center of the contact region under a perfectly conducting and grounded flat-ended punch with the radius of 25 nm and the indentation depth of 0.1 nm for varying pre-stretches as the function of the dimensionless electric displacement δ.

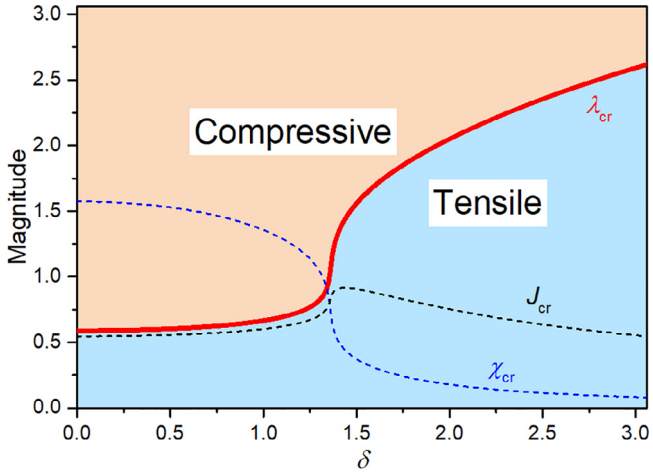

Fig. 6. Plot of the critical in-plane stretch (λ_{cr}), the critical vertical stretch (in the z-direction) (χ_{cr}) and the critical volume ratio (J_{cr}) as the function of the electric displacement (δ) for an SEA half-space indented by a perfectly conducting flat-ended punch.

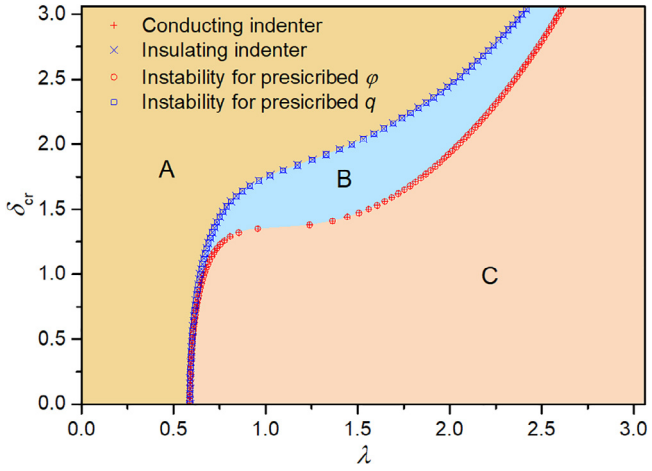

Fig. 7. Comparison between the critical basing field corresponding to zero incremental normal stress for perfectly conducting (or insulating) indentations and that for surface instability of a half-space with prescribed surface electric potential (φ = 0) (or surface free charge ($\dot{D}_{l0z} = 0$)).

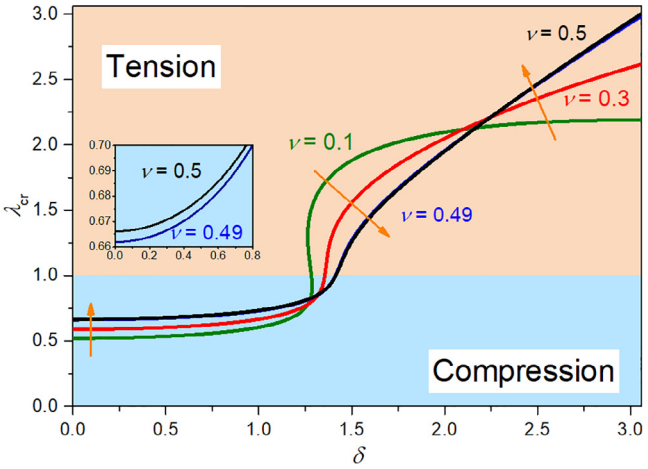

Fig. 8. Plot of the critical stretch (λ_{cr}) versus the dimensionless electric displacement (δ) of an SEA half-space under a perfectly conducting flat-ended circular punch for $\varepsilon = 1$ and various values of ν.

bility of the half-space. In particular, the half-space under tension can even lose its stability when the electric biasing field exceeds a critical value, regardless of the electric property of the punch. In Fig. 7, the stable region for prescribed surface electric potential (φ = 0) is denoted by C while that for prescribed surface free charge (q = constant) is B + C, and A is the common unstable region for both cases. It should be noted that a larger stable region indicates higher stability of the half-space. Thus, the half-space with an insulating surface is more stable than the half-space with its surface being electrically shorted.

Then, we examine the effects of compressibility and dielectric property on the instability of the SEA half-space. Fig. 8 presents the instability curves for the compressible half-space with three different values of Poisson's ratio (i.e. ν = 0.1, 0.3, 0.49). The results for the incompressible case ($\nu = 0.5$) obtained by Dorfmann and Ogden (2010a) are reproduced here for comparison. We can see that the effect of material compressibility on stability is not monotonic when the biasing electric displacement is also involved. For the case that the applied electric displacement is small ($\delta \leqslant\sim 1.25$) or sufficiently large ($\delta \geqslant\sim 2.2$), the half-space with larger ν will be more unstable. Otherwise ($\sim 1.25 < \delta <\sim 2.2$) the half-space with smaller ν is more susceptible to surface instability.

To investigate the effect of dielectric property on the surface instability of an SEA half-space, we take polydimethylsiloxane (PDMS) elastomer, a widely used electroactive elastomer, as an example. The dielectric property of PDMS elastomer varies with the type of cross-linker agent in the PDMS solution (Mark, 2009) and a high permittivity may be obtained by blending the elastomer with other polymers (Carpi et al., 2008b; Molberg et al., 2010), while the Poisson's ratio of the elastomer keeps almost unchanged (~0.5) (Wang and Krause, 1987). Fig. 9 shows the variation of the critical pre-stretch (λ_{cr}) with the dimensionless electric displacement of the PDMS half-space with fixed Poisson's ratio ($\nu = 0.4999$) for different dielectric constants (ε = 2.77, 2.8, 2.98 and 3.69) selected from Mark (2009). The gray curve ($\varepsilon = 1$) plotted for reference is very similar to the blue curve in Fig. 8, with only a tiny difference in the value of ν. As compared to the effect of compressibility, the effect of dielectric constant looks simpler that the PDMS elastomer with larger permittivity always leads to smaller λ_{cr} for a fixed biasing electric displacement. This effect is not obvious when the electric biasing field is small, while it gets enhanced as the electric displacement increases. Similar observations regarding the effects of

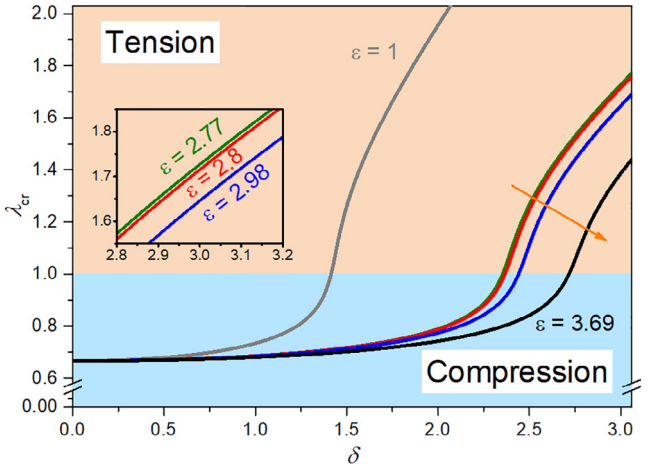

Fig. 9. Effect of the dielectric constant on the instability of an SEA half-space.

compressibility and dielectric property can be seen from Figs. E3 and E4 for the indentation by a perfectly insulating circular flat-ended punch.

4.3. Validity of linear indentation analysis for adhesive spherical contact

Since the SEA material is hyperelastic while the developed exact solutions are based on the linear incremental theory, it becomes very important to clarify under which conditions these solutions can be used to interpret the indentation responses. In this work, we assume that if the maximum strain during indentation is below 5%, then the linear indentation analysis is valid. This requirement can be easily met for the non-adhesive case by choosing proper penetration depth and indenter size, even at nanoscale. Taking the spherical indentation as an example, we show in Fig. F2(a) in Appendix F the variations of the dimensionless contact radius (a/R) and the incremental normal strain at the center of contact area (ε_z) with the dimensionless electric displacement (δ) for an SEA half-space under a perfectly conducting spherical punch of different sizes (R = 4, 160, 640 μm) but with a fixed indentation depth (4 nm). In this case, as shown in Fig. F1, the maximum indentation-induced strain is the incremental normal strain at

the center of the contact area (ε_z), which decreases with the increasing electric biasing field. The validity of the linear indentation analysis holds even when the radius of the indenter is as small as 4 μm.

However, when the adhesive interaction is introduced for two nontrivial values of the unit surface adhesion energy (Lu et al., 2011; Wu et al., 2011) as shown in Fig. F2(b) and (c), the incremental deformation becomes much larger than that of the non-adhesive case, unavoidably beyond the linear elastic regime (ε_z > 5%). In this case, we may suppress the deformation to some extent by enlarging the radius of the indenter, which can be manufactured up to 400 μm by the MEMS technology (Michałowski and Łuczak, 2018). Nevertheless, increasing the indenter size will lower the resolution and contrast of the indentation image. Fig. F2(d) indicates another strategy to keep the linear indentation analysis valid in a wide range of electric biasing field (from zero to the nearly critical value of instability) by reducing the surface adhesion energy per unit area (only 1‰ of those in Fig. F2(b) and (c)). The results presented in Figs. F3–F5 further show that both a/R and ε_z have a monotonously positive correlation with the magnitude of surface adhesion energy per unit area. It is noted that the surface adhesion energy can be easily tuned through surface treatment. As for a specific kind of SEA material, its adhesive interaction with the indenter varies and is affected by the composition of the indenter and/or surface chemistry of the coating of the probe tip (Lin and Horkay, 2008). In fact, proper modifications of the tip coating to regulate the probe-sample interaction have been repeatedly reported (Dos Santos Ferreira et al., 2010; Lei et al., 2018; Yam et al., 2003).

On the other hand, for spherical indentation, we have used a parabola to approximate the spherical profile in the analysis, which requires a small ratio between the indention depth or contact radius and the radius of indenter (i.e. a small d/R or a/R). For example, to keep the deviation of the two profiles (parabolic and spherical) smaller than 1%, d/R should be smaller than 4% or a/R should be smaller than 20% in the non-adhesive case. The conflict between the linear incremental model and the intrinsic large deformation characteristic of soft materials under adhesive contact emerges as a critical issue. A quantitative understanding of the validity of the linear indentation analysis for pre-deformed SEA materials is quite important but still lacking. In this sense, our exact solutions may help provide certain preliminary knowledge of the testing conditions under which the linear indentation analysis is applicable.

For the adhesive indentation test under diverse working conditions, it is interesting and necessary to find the critical value of unit surface adhesion energy when the incremental normal strain at the center of the contact area equals 5%. Fig. 10(a)–(c) plot the variations of the critical surface adhesion energy per unit area for an SEA half-space with varying dimensionless electric displacement.

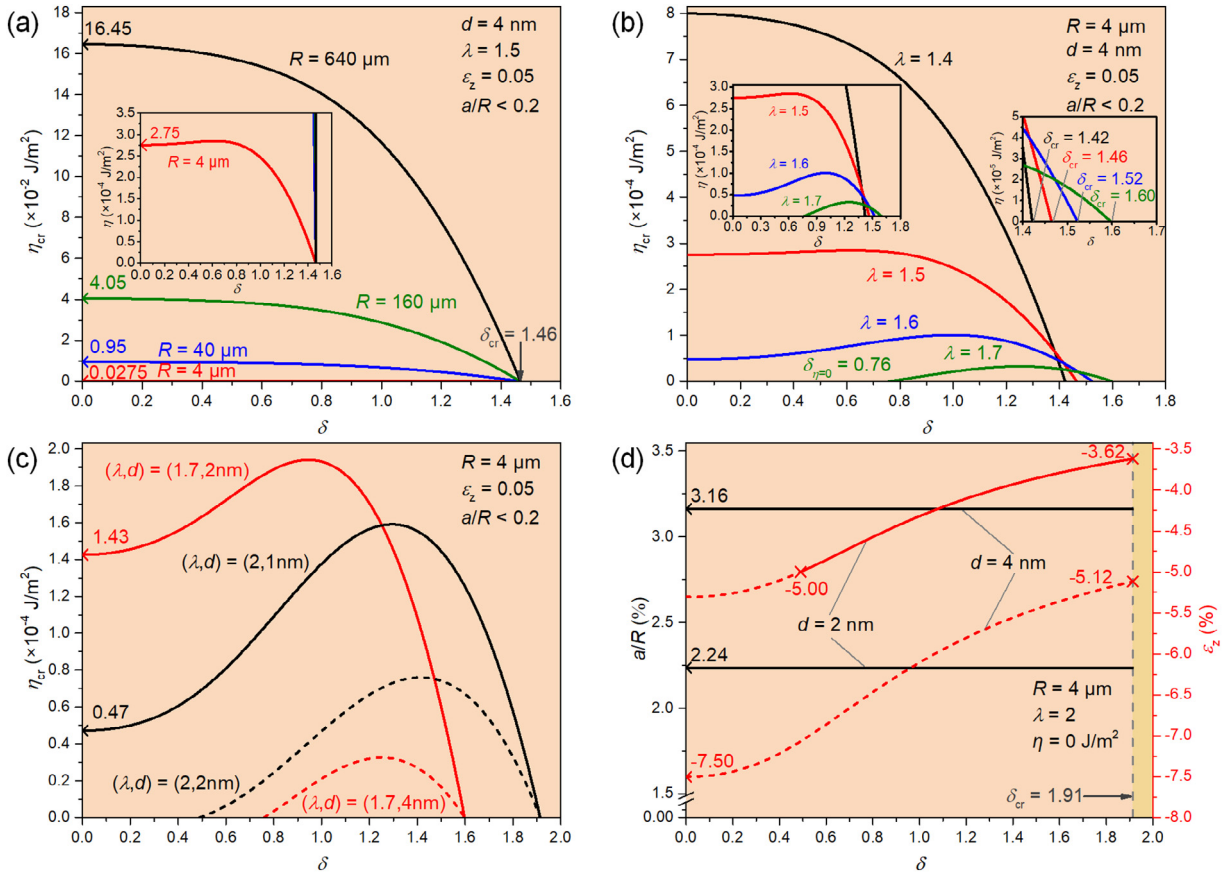

Fig. 10. Effect of the dimensionless electric displacement (δ) on the critical value of surface adhesion energy per unit area (η_{cr}) of perfectly conducting and grounded spherical indention of the SEA half-space under varying testing conditions and initial pre-stretches (λ): (a) different radii of indenters (R = 4, 40, 160, 640 μm) with fixed indentation depth (d = 4 nm) and pre-stretch (λ = 1.5); (b) different pre-stretches (λ = 1.4, 1.5, 1.6, 1.7) with fixed indentation depth (d = 4 nm) and radius of indenter (R = 4 μm); (c) different indentation depths (d = 1, 2, 4 nm) and pre-stretches (λ = 1.7, 2) with fixed indenter size (R = 4 μm); (d) variations of the non-adhesive dimensionless contact radius (a/R) and the incremental normal strain (ε_z) with dimensionless electric displacement (δ) for different indentation depths (d = 2, 4 nm) where the indenter size (R = 4 μm) and the pre-stretch (λ = 2) are fixed. The black solid lines in (d) describe the variations of the contact radius, and the red solid lines in (d) give those of the incremental normal strain within the linear elastic regime. The red dashed lines correspond to failure of the measurement and the vertical gray line shows the critical value of dimensionless electric displacement of surface instability. Both critical points are marked by crosses. Similar notations are implied unless stated otherwise.

The region below the solid curve of η_{cr} corresponds to the case $\varepsilon_z < 5\%$. The corresponding variations of a/R are provided in Fig. F6. The solid curves in Fig. 10(a) perfectly include all the critical points corresponding to $\varepsilon_z = 5\%$ in Figs. F2–F5, giving the guidance to choose a proper radius of the spherical indenter for a fixed indentation depth. As shown in Fig. 10(b), the SEA half-space bearing a larger pre-stretch usually should have a smaller critical unit surface adhesion energy when the electric biasing field applied is much smaller than the critical one. For the depth-fixed indentation, the half-space under a large pre-stretch may not have a critical surface adhesion energy per unit area until the dimensionless electric displacement reaches a threshold value ($\delta_{\eta=0}$), e.g. the case of λ = 1.7. The threshold value should not exceed the critical value of the electric biasing field for surface instability. If this condition is not satisfied, we can never perform an effective indentation test within the linear elastic regime, e.g. the case of λ = 2 as shown in Fig. 10(d) for d = 4 nm. For these two cases, we can solve this problem by properly decreasing the indentation depth. Fig. 10(c) shows that the value of critical surface adhesion energy per unit area is negatively correlated to the indentation depth. Besides, it always approaches zero when the half-space is subjected to the critical electric biasing field of instability.

4.4. More results for spherical and conical indentations

In this subsection, indentations by a spherical punch (R = 4 μm) and a conical punch ($\beta = 60°$) are, respectively, considered with the indentation depth of 4 nm to show the effect of adhesion on the indentation responses. The pre-stretch and applied electric displacement of the SEA half-space are fixed as $\lambda_1 = \lambda_2 = 1.5$, and $D_3 = 0.01\sqrt{\varepsilon_0\mu}$. The reduced unit adhesion energy $\eta_1 = 2.8 \times 10^{-5}$J/m^2 and $\eta_2 = 1.55 \times 10^{-4}$J/m^2 are adopted to account for the adhesive interaction during indentation.

We first focus on the perfectly conducting and grounded spherical punch ($\varphi_0 = 0$). As shown in Fig. 11(a), the adhesive effect makes an obvious difference on the distribution of the incremental vertical displacement (u_z) at the surface ($z = 0$). The adhesion-free contact response (black curve) is also presented in the figure for comparison. For adhesive contact (red and blue curves), the radius of contact area, which can be identified by the rising part of each curve, increases with the surface adhesion energy per unit area for a fixed indentation depth. Furthermore, although the distribution of the incremental vertical displacement inside the contact region should comply with the shape of the spherical punch, the outside distribution is highly affected by the surface adhesion. It is also seen that, when the surface adhesion energy decreases, the surface of the half-space outside the contact area may change from sinking to heaving.

Fig. 11(b) shows the distributions of the incremental radial displacement (u_ρ) at the surface for different values of the surface adhesion energy per unit area. The incremental radial displacement is rather small, more than one order of magnitude lower than the normal or vertical one. For adhesive contact, the distribution of the radial displacement inside the contact region looks not straightly correlated to the shape of the punch. This is quite expected because, in our analysis, we assume zero shear stress within the contact area though the adhesion energy has been taken into account. It is noted that the radial displacement first goes down from zero to negative. As the radial coordinate reaches a critical value, it turns to grow smoothly. Note that the maximum absolute value of the radial displacements within the contact region has a positive correlation with the magnitude of the surface adhesion energy per unit area (η). Outside the contact area, the effect of adhesion on the radial displacement is similar to that on the vertical displacement. As the radial coordinate becomes far away from the indenter, the incremental radial displacement gradually approaches zero, also as expected.

The adhesion also affects the distributions of the incremental stresses and electric displacements. Fig. 12 plots the distributions of the incremental normal stress (σ_{z1}) in the z-direction, the transverse shear stress ($\sigma_{\rho 2}$), the normal electric displacement (σ_{z2}) and the radial electric displacement ($\sigma_{\rho 3}$) at the surface for different values of surface adhesion energy per unit area (η). As is seen from Fig. 12, the maximum normal compressive stress and normal electric displacement always occur at the center of the contact region, of which the magnitudes are both positively correlated to the value of η. $\sigma_{\rho 2}$ has the same order of magnitude as σ_{z1} and linearly increases with the radial coordinate in the contact area, whether the adhesion is involved or not. We note that, as shown in Fig. 12, the nonzero incremental physical quantities all show a singular behavior at the contact edge when the surface adhesion energy is nonzero. It is simply because that the JKR model only accounts for the adhesive effect inside the contact region (Wu, 2012), leading to a physical discontinuity at the contact edge. To eliminate these singularities, we may need to utilize the MD model or take surface tension at the contact edge into consideration (Karpitschka et al., 2016).

Fig. 13 shows a comparison of the incremental vertical displacement at the surface between the modified JKR model and the traditional one under different values of the surface adhesion

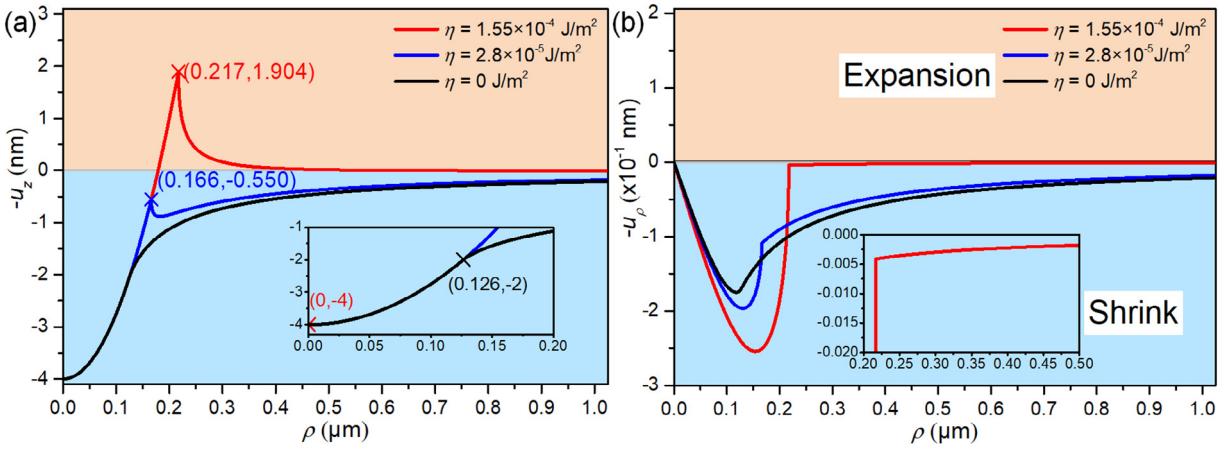

Fig. 11. Variations of the surface incremental (a) vertical displacement (u_z) and (b) radial displacement (u_ρ) for an SEA half-space under a perfectly conducting spherical punch (R = 4 μm, d = 4 nm) for different values of surface adhesion energy per unit area.

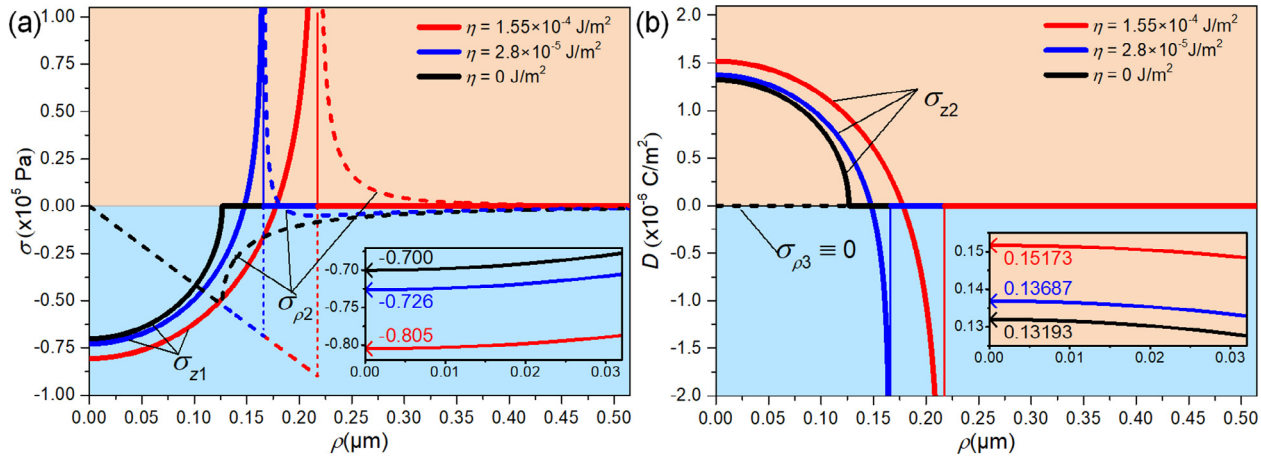

Fig. 12. Variations of the surface incremental (a) normal stress (σ_{z1}) and transverse shear stress ($\sigma_{\rho 2}$), and (b) normal electric displacement (σ_{z2}) and radial electric displacement ($\sigma_{\rho 3}$) for an SEA half-space under a perfectly conducting spherical punch (R = 4 μm, d = 40 nm) for different values of surface adhesion energy per unit area.

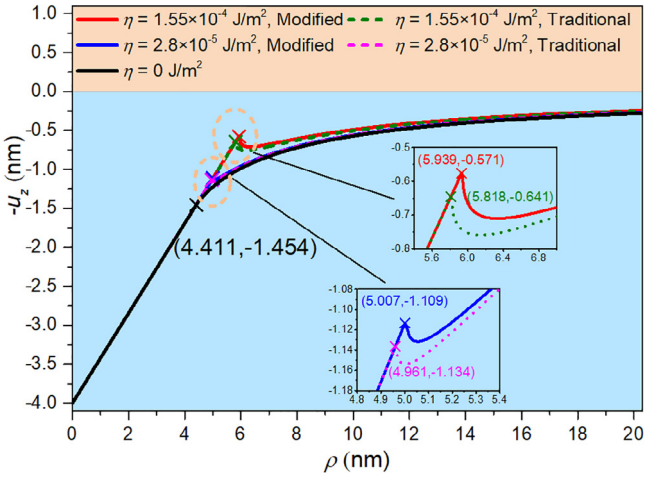

Fig. 13. Variations of incremental vertical displacement of an SEA half-space under a perfectly conducting conical punch (β = 60°) on the surface for different values of surface adhesion energy per unit area.

energy per unit area (η). For non-adhesive contact, the contact radius is calculated to be 4.411 nm. When $\eta = \eta_1$, the contact radii for the traditional and modified models are calculated to be 4.961 and 5.007 nm, respectively, whereas these are found to be 5.818 and 5.939 nm when $\eta = \eta_2$. Taking the value obtained by the modified JKR model as a reference, the relative deviations of the conventional model are about 0.92% and 2.04% for $\eta = \eta_1$ and $\eta = \eta_2$ respectively. We further calculate the point-wise incremental vertical displacement at the surface based on the two models. It is found that the relative deviations of the vertical displacement are up to 3.63% and 28.85%, respectively, for the two values of surface adhesion energy per unit area. These two kinds of deviations both show positive correlation with the magnitude of η. These results suggest that at least for a sharp-shaped punch (e.g. cone), the traditional model using the projected area may induce a large error of the surface displacement, which usually gives plenty of information in the indentation techniques. Thus, it becomes clear that the modified area should be used when the surface adhesion energy is involved.

5. Conclusions

In conclusion, we presented the exact solutions of 3D elastic and electric fields in terms of elementary functions for the adhesive contact between a pre-deformed soft electroactive half-space and an axisymmetric rigid indenter. The adhesion was considered by using the modified JKR model. We verified the theoretical solutions through comparison with FE simulations though only for a purely elastic neo-Hookean half-space. For the indentation of a compressible neo-Hookean electroactive half-space, the incremental normal stress may become tensile when the biasing electric displacement exceeds a critical value. This abnormal phenomenon was shown to be due to the occurrence of surface instability induced by the electric biasing field.

Numerical results show that the modification of contact area used in the calculation of surface adhesion energy is necessary at the micro- and nano-scales even if the adhesive effect is not very high. For the SEA materials with certain biasing states, in order to ensure the validity of SPM indentation tests within the linear elastic framework, the significant effects of electric biasing field and surface adhesion energy per unit area on the magnitude of incremental deformation were also carefully analyzed. The analysis provides a strategy to regulate the contact radius, by tuning the electric biasing field, with a fixed radius of indenter and/or a fixed indentation depth. As such, we believe that the adhesive contact solutions pave a right way for the nanoindentation technology or SPM to accurately characterize SEA materials in particular and a broad range of soft material systems with electromechanical couplings in general.

Declaration of Competing Interest

The authors declare that they have no known competing financial interests or personal relationships that could have appeared to influence the work reported in this paper.

Acknowledgments

The work was supported by the National Natural Science Foundation of China (Nos. 11532001 and 11621062). Partial supports from the Fundamental Research Funds for the Central Universities (No. 2016XZZX001-05), the Shenzhen Scientific and Technological Fund for R&D (No. JCYJ20170816172316775), 2019 Zhejiang University Academic Award for Outstanding Doctoral Candidates, Wenzhou City Huang Mengqi Dandelion Charitable Foundation, and China Scholarship Council are also acknowledged.

Appendix A. A summary of fundamental formulations

A.1. Nonlinear theory of electroelasticity

We here briefly recall the nonlinear theory of electroelasticity and the incremental field theory proposed by Dorfmann and Ogden (2010b). Beginning with an SEA body occupying a region B_r with boundary ∂B_r in the undistorted reference configuration, we denote a material point in B_r by its position vector $\boldsymbol{X}$. The body is then subjected to a certain static deformation as well as an electric displacement field, and as a result, the material point will move to a new position $\boldsymbol{x}$ such that the body occupies a new region B with boundary ∂B in the current configuration. The overall deformation of the body can be defined via a smooth function $\boldsymbol{x}=\chi(\boldsymbol{X})$. The deformation gradient is then given by $\boldsymbol{F}=\mathrm{Grad}\chi$, where Grad is the gradient operator in B_r, and the volume ratio is $J=\det\boldsymbol{F}$. The left and right Cauchy-Green tensors associated with $\boldsymbol{F}$ are denoted by $\boldsymbol{b}=\boldsymbol{F}\boldsymbol{F}^{\mathrm{T}}$ and $\boldsymbol{c}=\boldsymbol{F}^{\mathrm{T}}\boldsymbol{F}$, respectively, where the superscript T denotes transpose operation. We may describe the properties of the SEA body by introducing an energy density function $\Omega=\Omega(\boldsymbol{F},\boldsymbol{D}_l)$, satisfying $\Omega(\boldsymbol{I},0)=0$ without loss of generality, where $\boldsymbol{D}_l$ is the electric displacement vector in B_r. The nonlinear constitutive relations are then expressed by

$$\boldsymbol{T}=\frac{\partial\Omega}{\partial\boldsymbol{F}},\qquad \boldsymbol{E}_l=\frac{\partial\Omega}{\partial\boldsymbol{D}_l}, \tag{A1}$$

where the nominal stress tensor $\boldsymbol{T}$ is related to the total Cauchy stress $\boldsymbol{\tau}$ through $\boldsymbol{T}=J\boldsymbol{F}^{-1}\boldsymbol{\tau}$, and the nominal electric field vector is connected with the true one by $\boldsymbol{E}_l=\boldsymbol{F}^{\mathrm{T}}\boldsymbol{E}$. For isotropic materials, we have

$$\begin{aligned}
&J\boldsymbol{\tau}=2\Omega_1\boldsymbol{b}+2\Omega_2\left(I_1\boldsymbol{b}-\boldsymbol{b}^2\right)+2I_3\Omega_3\boldsymbol{I}+2J^2\Omega_5\boldsymbol{D}\otimes\boldsymbol{D}\\
&\quad+2\Omega_6J^2(\boldsymbol{D}\otimes\boldsymbol{b}\boldsymbol{D}+\boldsymbol{b}\boldsymbol{D}\otimes\boldsymbol{D}),\\
&J\tau_{ji}=2\Omega_1b_{ji}+2\Omega_2\left(I_1b_{ji}-b_{jk}b_{ki}\right)+2\Omega_3I_3\delta_{ji}+2J^2\Omega_5D_jD_i\\
&\quad+2\Omega_6J^2\left(D_jb_{ik}D_k+b_{jk}D_kD_i\right),\\
&\boldsymbol{E}=2J\left(\Omega_4\boldsymbol{b}^{-1}\boldsymbol{D}+\Omega_5\boldsymbol{D}+\Omega_6\boldsymbol{b}\boldsymbol{D}\right),\\
&E_k=2J\left(\Omega_4b_{ki}^{-1}D_i+\Omega_5D_k+\Omega_6b_{ik}D_i\right),
\end{aligned} \tag{A2}$$

where i, j, k = 1, 2, 3, $\Omega_m=\partial\Omega/\partial I_m(m=1,2,\ldots,6)$, and $I_1=\mathrm{tr}\boldsymbol{c}$, $I_2=[(\mathrm{tr}\boldsymbol{c})^2-\mathrm{tr}(\boldsymbol{c}^2)]/2$, $I_3=\det\boldsymbol{c}$, $I_4=\boldsymbol{D}_l\cdot\boldsymbol{D}_l$, $I_5=\boldsymbol{D}_l\cdot(\boldsymbol{c}\boldsymbol{D}_l)$, $I_6=\boldsymbol{D}_l\cdot(\boldsymbol{c}^2\boldsymbol{D}_l)$ are the six independent invariants. The governing equations read as

$$\mathrm{Div}\boldsymbol{T}=\boldsymbol{0},\qquad \mathrm{Curl}\boldsymbol{E}_l=\boldsymbol{0},\qquad \mathrm{Div}\boldsymbol{D}_l=0, \tag{A3}$$

If there is no electric field outside the SEA body, the natural boundary conditions are

$$\boldsymbol{\tau}\boldsymbol{n}=\boldsymbol{t}_a,\qquad \boldsymbol{n}\cdot\boldsymbol{D}=q_0,\qquad \boldsymbol{n}\times\boldsymbol{E}=\boldsymbol{0},\quad(\text{on }\partial B) \tag{A4}$$

where $\boldsymbol{t}_a$ and q_0 are the applied surface traction and the prescribed charge density on ∂B.

An infinitesimal deformation $\dot{\boldsymbol{x}}(\boldsymbol{X})$ is assumed to be superimposed on the finite static deformation $\boldsymbol{x}=\chi(\boldsymbol{X})$. Here and below we follow the notations adopted by Dorfmann and Ogden (2010b). In particular, the dotted variables represent the incremental quantities. The Eulerian forms of equilibrium equations of the incremental motion are

$$\mathrm{div}\dot{\boldsymbol{T}}_0=\boldsymbol{0},\qquad \mathrm{div}\dot{\boldsymbol{D}}_{l0}=0,\qquad \mathrm{curl}\dot{\boldsymbol{E}}_{l0}=\boldsymbol{0}, \tag{A5}$$

where $\dot{\boldsymbol{T}}_0$, $\dot{\boldsymbol{D}}_{l0}$ and $\dot{\boldsymbol{E}}_{l0}$ are "push-forward" version of the incremental stress, electric displacement, and electric field, respectively. The incremental constitutive relations read

$$\dot{\boldsymbol{T}}_0=\mathscr{A}_0\boldsymbol{H}+\boldsymbol{\Gamma}_0\dot{\boldsymbol{D}}_{l0},\qquad \dot{\boldsymbol{E}}_{l0}=\boldsymbol{\Gamma}_0^{\mathrm{T}}\boldsymbol{H}+\boldsymbol{K}_0\dot{\boldsymbol{D}}_{l0}, \tag{A6}$$

where $\mathscr{A}_0$, $\boldsymbol{\Gamma}_0$ and $\boldsymbol{K}_0$ are the fourth-, third-, and second-order effective or instantaneous material tensors, respectively, with the following component forms for an isotropic SEA half-space

$$\begin{aligned}
&\mathscr{A}_{0piqj}=J^{-1}F_{p\alpha}F_{q\beta}\left(\sum_{m=1,m\neq4}^{6}\sum_{n=1,n\neq4}^{6}\Omega_{mn}\frac{\partial I_m}{\partial F_{i\alpha}}\frac{\partial I_n}{\partial F_{j\beta}}+\sum_{m=1,m\neq4}^{6}\Omega_m\frac{\partial^2I_m}{\partial F_{i\alpha}\partial F_{j\beta}}\right)=\mathscr{A}_{0qjpi},\\
&\Gamma_{0piq}=F_{p\alpha}F_{\beta q}^{-1}\left(\sum_{m=1}^{6}\sum_{n=1,n\neq4}^{6}\Omega_{mn}\frac{\partial I_m}{\partial F_{i\alpha}}\frac{\partial I_n}{\partial D_{l\beta}}+\sum_{m=5}^{6}\Omega_m\frac{\partial^2I_m}{\partial F_{i\alpha}\partial D_{l\beta}}\right)=\Gamma_{0ipq},\\
&K_{0pg}=JF_{\alpha p}^{-1}F_{\beta g}^{-1}\left(\sum_{m=4}^{6}\sum_{n=4}^{6}\Omega_{mn}\frac{\partial I_m}{\partial D_{l\alpha}}\frac{\partial I_n}{\partial D_{l\beta}}+\sum_{m=4}^{6}\Omega_m\frac{\partial^2I_m}{\partial D_{l\alpha}\partial D_{l\beta}}\right)=K_{0gp},
\end{aligned} \tag{A7}$$

where $\Omega_{mn}=\partial^2\Omega/(\partial I_m\partial I_n)$. The Roman and Greek subscripts correspond to the reference and current configurations, respectively. $\boldsymbol{H}=\mathrm{grad}\boldsymbol{u}$ is the displacement gradient with respect to $\boldsymbol{x}$, and $\boldsymbol{u}=\dot{\boldsymbol{x}}(\boldsymbol{X})=\boldsymbol{u}(\boldsymbol{x})$ is the incremental displacement vector. Here and after, the Einstein summation convention is implied unless otherwise stated.

Since the effect of the external electric field can be ignored (Ericksen, 2007; Suo et al., 2008; Zhang et al., 2012), the incremental boundary conditions are given by

$$\dot{\boldsymbol{T}}_0^{\mathrm{T}}\boldsymbol{n}=\dot{\boldsymbol{t}}_{A0},\qquad \boldsymbol{n}\cdot\dot{\boldsymbol{D}}_{l0}=\dot{q}_{A0},\qquad \boldsymbol{n}\times\dot{\boldsymbol{E}}_{l0}=\boldsymbol{0}, \tag{A8}$$

where $\dot{\boldsymbol{t}}_{A0}$ denotes the incremental mechanical traction and $\dot{q}_{A0}$ is the incremental electric charge per unit area on ∂B.

A.2. General solution for a pre-deformed SEA body

By introducing an electric potential φ and letting $\dot{\boldsymbol{E}}_{l0}=-\mathrm{grad}\varphi$, the third equation in Eq. (A5) can be satisfied. Then, for an isotropic SEA material with the finite pre-deformation described in Eq. (1), we can rewrite the constitutive equations in Eq. (A6) in the new form of Eqs. (2) and (3) (Zhang et al., 2012). The effective material constants there can be related to the instantaneous material constants in Eq. (A7) as

$$\begin{aligned}
&\varepsilon_{11}=1/K_{011},\quad \varepsilon_{33}=1/K_{033},\\
&e_{15}=-\varepsilon_{11}\Gamma_{0131},\quad e_{31}=-\varepsilon_{33}\Gamma_{0113},\quad e_{33}=-\varepsilon_{33}\Gamma_{0333},\\
&c_{11}=\mathscr{A}_{01111}+\Gamma_{0113}e_{31},\quad c_{12}=\mathscr{A}_{01122}+\Gamma_{0113}e_{31},\\
&c_{13}=\mathscr{A}_{01133}+\Gamma_{0113}e_{33},\quad c_{33}=\mathscr{A}_{03333}+\Gamma_{0333}e_{33},\\
&c_{58}=\mathscr{A}_{01331}+\Gamma_{0131}e_{15},\quad c_{55}=\mathscr{A}_{01313}+\Gamma_{0131}e_{15},\\
&c_{88}=\mathscr{A}_{03131}+\Gamma_{0131}e_{15},\quad c_{69}=\mathscr{A}_{01221},\quad c_{66}=\mathscr{A}_{01212}.
\end{aligned} \tag{A9}$$

All non-zero material parameters for an isotropic SEA material are given explicitly in Appendix B.1.

As mentioned in the text, the general solution to the governing equations (i.e. Eqs. (2), (3) and (A5)) can be expressed in terms of three quasi-harmonic functions ψ_i ($i=1,\ 2,\ 3$)), which satisfy

$$\left(\Delta+\frac{\partial^2}{\partial z_i^2}\right)\psi_i=0\ , \tag{A10}$$

where Δ is the two-dimensional Laplace operator in the ρ-ϕ plane, and $z_i=s_ix_3$ ($i=1,2,3$), with s_1, s_2 and s_3 being the roots of the characteristic equation below

$$n_0 s^6 - n_1 s^4 + n_2 s^2 - n_3 = 0, \tag{A11}$$

where

$$\begin{aligned}
n_0 &= c_{88}(e_{33}^2 + c_{33}\varepsilon_{33}),\\
n_1 &= c_{33}[(e_{15}+e_{31})^2 + c_{88}\varepsilon_{11} + c_{11}\varepsilon_{33}] + \varepsilon_{33}[c_{55}c_{88} - (c_{13}+c_{58})^2]\\
&\quad + e_{33}[2c_{88}e_{15} + c_{11}e_{33} - 2(e_{15}+e_{31})(c_{13}+c_{58})],\\
n_2 &= \varepsilon_{11}[c_{11}c_{33} + c_{55}c_{88} - (c_{13}+c_{58})^2] + c_{55}e_{31}^2 + c_{11}c_{55}\varepsilon_{33}\\
&\quad + e_{15}[2c_{11}e_{33} - 2c_{13}e_{15} - 2(c_{13}+c_{58}-c_{55})e_{31} - (2c_{58} - c_{55} - c_{88})e_{15}],\\
n_3 &= c_{11}(e_{15}^2 + c_{55}\varepsilon_{11}).
\end{aligned} \tag{A12}$$

The coefficients in Eqs. (4) and (5) are given by

$$\alpha_{1i} = \frac{c_{11}\varepsilon_{11} - m_3 s_i^2 + c_{88}\varepsilon_{33}s_i^4}{(m_1 - m_2 s_i^2)s_i}, \qquad \alpha_{2i} = \frac{c_{11}e_{15} - m_4 s_i^2 + c_{88}e_{33}s_i^4}{(m_1 - m_2 s_i^2)s_i}, \tag{A13}$$

$$\begin{aligned}
&\gamma_{1i} = \alpha_{1i}c_{33}s_i + \alpha_{2i}e_{33}s_i - c_{13}, \varpi_{1i} = c_{88}s_i + c_{58}\alpha_{1i} + e_{15}\alpha_{2i},\\
&\gamma_{2i} = (\alpha_{1i}e_{33} - \alpha_{2i}\varepsilon_{33})s_i - e_{31}, \varpi_{2i} = c_{58}s_i + c_{55}\alpha_{1i} + e_{15}\alpha_{2i},\\
&\gamma_{3i} = 2(\alpha_{1i}c_{13} + \alpha_{2i}e_{31})s_i - (c_{11}+c_{12}), \quad \varpi_{3i} = e_{15}(s_i + \alpha_{1i}) - \varepsilon_{11}\alpha_{2i}.
\end{aligned} \tag{A14}$$

where

$$\begin{aligned}
&m_1 = \varepsilon_{11}(c_{13}+c_{58}) + e_{15}(e_{15}+e_{31}), \quad m_2 = \varepsilon_{33}(c_{13}+c_{58}) + e_{33}(e_{15}+e_{31}),\\
&m_3 = c_{11}\varepsilon_{33} + c_{88}\varepsilon_{11} + (e_{15}+e_{31})^2, \; m_4 = c_{11}e_{33} + c_{88}e_{15} - (c_{13}+c_{58})(e_{15}+e_{31}),
\end{aligned} \tag{A15}$$

As can be seen, the coefficients in Eqs. (4) and (5) are all combinations of the effective material constants in Eq. (A9).

It should be noted that Eqs. (4) and (5) are valid only when the characteristic equation has three distinct roots. For cases of equal roots, the form of the general solution shall be changed accordingly (Ding et al., 2006). The explicit expressions of s_1, s_2 and s_3 can be readily obtained, just as for incompressible materials. It is noted that the roots may become imaginary, which corresponds to the situation that the material loses stability (Dorfmann and Ogden, 2010a). In this paper, proper pre-deformations are assumed such that $Re(s_i) > 0$ always holds.

A.3. Conducting indenters

A.3.1. Potential theory method

For perfectly conducting indenters, we assume:

$$\psi_i(z) = \sum_{j=1}^{2} h_{ij} H_j(z_i), \quad (i = 1,2,3) \tag{A16}$$

where h_{ij} $(i = 1,\ 2,\ 3; j = 1,\ 2)$ are undetermined constants, and

$$H_j(\rho,\phi,z) = \int_0^{2\pi}\int_0^a \ln[R(M,N) + z]\sigma_{zj}(N) r \mathrm{d}r\mathrm{d}\theta, \qquad (j = 1,2) \tag{A17}$$

with $\sigma_{zj}(N)$ being the value of stress (for j = 1) or electric displacement (for j = 2) at the position $N(r,\theta,0)$, an arbitrary point in the contact region, and $R(M,N)$ is the distance between any position in the half-space denoted by $M(\rho,\phi,z)$ and $N(r,\theta,0)$.

According to the properties of a single-layer potential, its second derivative satisfies

$$\partial^2 H_j/\partial z^2|_{z=0} = -2\pi\sigma_{zj}|_{z=0}. \tag{A18}$$

Then, in conjugation with the third condition in Eq. (7), we may set

$$\begin{aligned}
&\sum_{i=1}^{3} h_{ij}\gamma_{ki} = -\delta_{jk}(2\pi)^{-1},\\
&\sum_{i=1}^{3} h_{ij}\varpi_{1i} = 0, \qquad (j,k = 1,2)
\end{aligned} \tag{A19}$$

where h_{ij} then can be obtained from Eq. (A19), and their complicit expressions are given in Appendix B.2. The vertical displacement (for k = 1) and the electric potential (for k = 2) within the contact region can also be written as, in view of Eqs. (A16) and (4)

$$w_k(N_0) = \sum_{j=1}^{2} g_{jk}\int_0^{2\pi}\int_0^a \frac{\sigma_{zj}(N)}{R(N_0,N)} r\mathrm{d}r\mathrm{d}\theta, \quad (k = 1,2) \tag{A20}$$

where $N_0(r_0,\theta_0,0)$ is also an arbitrary point in the contact area, and

$$g_{jk} = \sum_{i=1}^{3} h_{ij}\alpha_{ki}, \quad (j,k = 1,\ 2) \tag{A21}$$

As for the axisymmetric problems, solving Eq. (A20) yields the incremental normal stress and electric displacement on the surface as

$$\sigma_{zj}(\rho,\phi,0) = \frac{1}{\pi^2}\left[\frac{\chi_j(a)}{\sqrt{a^2-\rho^2}} - \int_\rho^a \frac{\chi_j'(\tau)}{\sqrt{\tau^2-\rho^2}}\mathrm{d}\tau\right], \tag{A22}$$

where

$$\chi_j(t) = \int_0^t \frac{x\times\omega_j(x)\mathrm{d}x}{t\sqrt{t^2-x^2}} + \int_0^t \frac{x^2\omega_j'(x)\mathrm{d}x}{t\sqrt{t^2-x^2}}, \tag{A23}$$

with

$$\begin{cases}
\omega_1(N_0) = \frac{g_{22}w_1(N_0) - g_{21}w_2(N_0)}{A_0},\\
\omega_2(N_0) = \frac{g_{11}w_2(N_0) - g_{12}w_1(N_0)}{A_0},
\end{cases} \qquad A_0 = g_{11}g_{22} - g_{12}g_{21}. \tag{A24}$$

Integrating Eq. (A22) over the contact area gives the total force (for j = 1) and total charge (for j = 2) applied on the punch as

$$p_j^{\mathrm{C}} = -2\pi\int_0^a \sigma_{zj}(\rho,\phi,0)\rho\mathrm{d}\rho = -\frac{2}{\pi}\int_0^a \chi_j(t)\mathrm{d}t, \qquad (j = 1,\ 2) \tag{A25}$$

where the superscript C represents the conducting indenter.

A.3.2. Modified JKR model

We define the stress and electric displacement intensity factors at the contact edge, denoted as K_1^{C} and K_2^{C}, by

$$K_j^{\mathrm{C}} = \lim_{\rho\to a}\left[\sqrt{2\pi(a-\rho)}\sigma_{zj}(\rho,\phi,0)\right] = \frac{1}{\pi\sqrt{\pi a}}\chi_j(a). \qquad (j = 1,\ 2) \tag{A26}$$

The relation of the two intensity factors can be obtained from Eqs. (A23) and (A26) as

$$K_2^{\mathrm{C}} = \frac{\varphi_0}{g_{22}\pi\sqrt{\pi a}} - \frac{g_{12}}{g_{22}}K_1^{\mathrm{C}}. \tag{A27}$$

Eq. (A22) can be rewritten as, in view of Eq. (A26),

$$\sigma_{zj}(\rho,\phi,0) = \sqrt{\frac{a}{\pi}}\frac{K_j^{\mathrm{C}}}{\sqrt{a^2-\rho^2}} - \frac{1}{\pi^2}\int_\rho^a \frac{\chi_j'(\tau)}{\sqrt{\tau^2-\rho^2}}\mathrm{d}\tau. \tag{A28}$$

Following the process of Maugis (2000), the unloading of the indenter is analogous to a crack problem. For the punch to depart from the surface, the mechanical energy release rate at the edge of the contact area (G_{M}) may be expressed as

$$G_{\mathrm{M}} = \lim_{\Delta a\to 0}\frac{1}{\Delta a}\int_0^{\Delta a}\frac{1}{2}\sigma_{z1}(a-\Delta\rho,\phi,0)[w_1](a+\Delta\rho,\phi,0)\mathrm{d}x, \tag{A29}$$

where Δa is the crack extension. The incremental normal stress (σ_{z1}), and the incremental displacement discontinuity $[w_1]$ in the vicinity of the contact edge can be asymptotically obtained as

$$\begin{cases} \sigma_{z1}(a-\Delta\rho,\theta,0)=\frac{K_1^C}{\sqrt{2\pi\Delta\rho}}, \\ [w_1](a+\Delta\rho,\theta,0)\simeq -4\pi\left(g_{11}K_1^C+g_{21}K_2^C\right)\sqrt{\frac{\Delta\rho}{2\pi}}, \end{cases} \tag{A30}$$

where $\Delta\rho$ is a small quantity. Then, the expression of G_M is obtained as

$$G_M=-\frac{\pi}{2}K_1^C\left(g_{11}K_1^C+g_{21}K_2^C\right), \tag{A31}$$

or

$$G_M=-\frac{\pi A_0}{2g_{22}}K_1^C\left(K_1^C+\frac{g_{21}\varphi_0}{A_0\pi\sqrt{\pi a}}\right). \tag{A32}$$

The equilibrium condition during adhesive contact requires (Lu et al., 2011)

$$\left(G_M-\eta\frac{\partial S}{\partial S_p}\right)\mathrm{d}S_p=0, \tag{A33}$$

where η is the surface adhesion energy per unit area, $S_p=\pi a^2$ is the projected area of the real contact area (S), and we have the ratio $(\partial S/\partial S_p)$ at $\rho=a$ as

$$\frac{\partial S}{\partial S_p}=\sqrt{1+\left[f'(a)\right]^2}. \tag{A34}$$

We then get from Eqs. (A33) and (A34)

$$G_M=\eta\sqrt{1+\left[f'(a)\right]^2}. \tag{A35}$$

Finally, substitution of Eq. (A32) into Eq. (A35) gives the explicit relation between the stress intensity factor and the modified surface adhesion energy per unit area ($\eta^*=\eta\sqrt{1+\left[f'(a)\right]^2}$) as

$$-\frac{\pi A_0}{2g_{22}}K_1^C\left(K_1^C+\frac{g_{21}\varphi_0}{A_0\pi\sqrt{\pi a}}\right)=\eta^*, \tag{A36}$$

or

$$K_1^C=\frac{1}{2A_0\pi\sqrt{\pi a}}\left[\sqrt{\left(g_{21}\varphi_0\right)^2-8a\pi^2A_0g_{22}\eta^*}-g_{21}\varphi_0\right]. \tag{A37}$$

A.3.3. Indentation analysis

For axisymmetric and conducting indenters, Eq. (A25) may be rewritten as

$$\begin{cases} p_1^C=-\frac{2g_{22}a}{\pi A_0}\left(d-\frac{g_{21}}{g_{22}}\varphi_0\right)+\frac{2g_{22}}{\pi A_0}\int_0^a\sqrt{a^2-\rho^2}f'(\rho)\mathrm{d}\rho, \\ p_2^C=\frac{2g_{12}a}{\pi A_0}\left(d-\frac{g_{11}}{g_{12}}\varphi_0\right)-\frac{2g_{12}}{\pi A_0}\int_0^a\sqrt{a^2-\rho^2}f'(\rho)\mathrm{d}\rho. \end{cases} \tag{A38}$$

To derive the above equation, the following expressions from Eq. (A23) have been utilized

$$\begin{cases} \chi_1(t)=\frac{g_{22}d-g_{21}\varphi_0}{A_0}-\frac{g_{22}t}{A_0}\int_0^t\frac{f'(\rho)\mathrm{d}\rho}{\sqrt{t^2-\rho^2}}, \\ \chi_2(t)=\frac{-g_{12}d+g_{11}\varphi_0}{A_0}+\frac{g_{12}t}{A_0}\int_0^t\frac{f'(\rho)\mathrm{d}\rho}{\sqrt{t^2-\rho^2}}. \end{cases} \tag{A39}$$

Especially, substitution of $\chi_1(a)$ into Eq. (A26) yields the depth-radius relation

$$d=\frac{A_0\pi\sqrt{\pi a}K_1^C+g_{21}\varphi_0}{g_{22}}+\int_0^a\frac{af'(\rho)\mathrm{d}\rho}{\sqrt{a^2-\rho^2}}, \tag{A40}$$

where the expression of K_1^C is given in Eq. (A37). Equation (A38) may be subsequently rewritten as

$$\begin{cases} p_1^C=-\frac{2g_{22}}{\pi A_0}\int_0^a\frac{x^2f'(x)}{\sqrt{a^2-x^2}}\mathrm{d}x-\frac{\sqrt{\left(g_{21}\varphi_0\right)^2-8a\pi^2A_0g_{22}\eta^*}-g_{21}\varphi_0}{\pi A_0a^{-1}}, \\ p_2^C=\frac{2g_{12}}{\pi A_0}\int_0^a\frac{x^2f'(x)}{\sqrt{a^2-x^2}}\mathrm{d}x-\frac{(2g_{11}g_{22}-g_{12}g_{21})a\varphi_0}{\pi A_0g_{22}}+\frac{g_{12}\sqrt{\left(g_{21}\varphi_0\right)^2-8a\pi^2A_0g_{22}\eta^*}}{\pi A_0g_{22}a^{-1}}. \end{cases} \tag{A41}$$

Furthermore, for any conducting indenter with its shape described by Eq. (6), we can derive the explicit load–displacement relation as follows

$$d=-\frac{\pi A_0}{2ag_{22}}p_1^C+\frac{g_{21}}{g_{22}}\varphi_0+\sqrt{\pi}\sum_{n=1}^{\infty}\frac{\Gamma(\frac{n}{2}+1)}{\Gamma(\frac{n+1}{2})}r_na^n. \tag{A42}$$

Accordingly, Eqs. (A39) and (A41) respectively become

$$\begin{cases} \chi_1(a)=\frac{g_{22}}{A_0}\left(d-\sqrt{\pi}\sum_{n=1}^{\infty}\frac{\Gamma(\frac{n}{2}+1)}{\Gamma(\frac{n+1}{2})}r_na^n\right)-\frac{g_{21}}{A_0}\varphi_0, \\ \chi_2(a)=\frac{-g_{12}}{A_0}\left(d-\sqrt{\pi}\sum_{n=1}^{\infty}\frac{\Gamma(\frac{n}{2}+1)}{\Gamma(\frac{n+1}{2})}r_na^n\right)-\frac{g_{11}}{A_0}\varphi_0, \end{cases} \tag{A43}$$

and

$$\begin{cases} p_1^C=-\frac{2ag_{22}}{\sqrt{\pi}A_0}\sum_{n=1}^{\infty}\frac{n\Gamma(\frac{n}{2}+1)}{(n+1)\Gamma(\frac{n+1}{2})}r_na^n \\ \qquad -\frac{\sqrt{\left(g_{21}\varphi_0\right)^2-8a\pi^2A_0g_{22}\eta\sqrt{1+\left(\sum_{n=1}^{\infty}nr_na^{n-1}\right)^2}}-g_{21}\varphi_0}{\pi A_0a^{-1}}, \\ p_2^C=\frac{2ag_{12}}{\sqrt{\pi}A_0}\sum_{n=1}^{\infty}\frac{n\Gamma(\frac{n}{2}+1)}{(n+1)\Gamma(\frac{n+1}{2})}r_na^n-\frac{(2g_{11}g_{22}-g_{12}g_{21})a\varphi_0}{\pi A_0g_{22}} \\ \qquad +\frac{g_{12}\sqrt{\left(g_{21}\varphi_0\right)^2-8a\pi^2A_0g_{22}\eta\sqrt{1+\left(\sum_{n=1}^{\infty}nr_na^{n-1}\right)^2}}}{\pi A_0g_{22}a^{-1}}. \end{cases} \tag{A44}$$

Thus, once the values of p_1^C and φ_0 (or p_2^C), r_n, surface adhesion energy per unit area (η) and related material constants are given, the contact radius (a) can be determined from Eq. (A44). For example, for punches with smooth profiles (spherical and conical) subject to a prescribed electric potential (φ_0), setting $p_1^C=0$ gives the following equation as

$$\frac{\sum_{n=1}^{\infty}\frac{n\Gamma(\frac{n}{2}+1)}{(n+1)\Gamma(\frac{n+1}{2})}r_na_0^{n-1}}{\sqrt{1+\left(\sum_{n=1}^{\infty}nr_na_0^{n-1}\right)^2}}=\frac{2\pi A_0\eta}{\frac{g_{21}\varphi_0}{\sqrt{\pi}}-g_{22}\sum_{n=1}^{\infty}\frac{n\Gamma(\frac{n}{2}+1)}{(n+1)\Gamma(\frac{n+1}{2})}r_na_0^n}, \tag{A45}$$

from which the radius of contact area induced by adhesion (a_0) may be found.

A.4. Insulating indenters

A.4.1. Potential theory method

For perfectly insulating indenters, the analysis procedure is quite similar to that presented in Appendix A.3. We now assume

$$\psi_i(z)=h_{i1}H_1(z_i)\ . \qquad (i=1,2,3) \tag{A46}$$

Then one may obtain, analogous to Eq. (A22), the following formula

$$\sigma_{z1}(\rho,\phi,0)=\frac{1}{\pi^2}\left[\frac{\chi_0(a)}{\sqrt{a^2-\rho^2}}-\int_\rho^a\frac{\chi_0'(\tau)}{\sqrt{\tau^2-\rho^2}}\mathrm{d}\tau\right], \tag{A47}$$

with

$$\chi_0(t)=\int_0^t\frac{x\times\omega_0(x)\mathrm{d}x}{t\sqrt{t^2-x^2}}+\int_0^t\frac{x^2\omega_0'(x)\mathrm{d}x}{t\sqrt{t^2-x^2}},\ \omega_0(N_0)=\frac{w_1(N_0)}{g_{11}}. \tag{A48}$$

The corresponding stress intensity factor is

$$K_1^{\mathrm{I}} = \lim_{\rho\to a}\left[\sqrt{2\pi(a-\rho)}\sigma_{z1}(\rho,\theta,0)\right] = \frac{1}{\pi\sqrt{\pi a}}\chi_0(a)\ , \tag{A49}$$

where the superscript I represents the insulating indenter. Then Eq. (A47) can be rewritten as

$$\sigma_{z1}(\rho,\phi,0) = \sqrt{\frac{a}{\pi}}\frac{K_1^{\mathrm{I}}}{\sqrt{a^2-\rho^2}} - \frac{1}{\pi^2}\int_\rho^a \frac{\chi_0'(\tau)}{\sqrt{\tau^2-\rho^2}}\mathrm{d}\tau, \tag{A50}$$

and the total force is given by

$$p_1^{\mathrm{I}} = -2\pi\int_0^a \sigma_{z1}(\rho,\phi,0)\rho\mathrm{d}\rho = -\frac{2}{\pi}\int_0^a \chi_0(t)\mathrm{d}t. \tag{A51}$$

A.4.2. Modified JKR model

Correspondingly, the relation between the stress intensity factor and the modified surface adhesion energy per unit area is

$$-\frac{\pi g_{11}}{2}\left(K_1^{\mathrm{I}}\right)^2 = \eta^*, \tag{A52}$$

or

$$K_1^{\mathrm{I}} = \sqrt{-\frac{2}{\pi g_{11}}\eta^*}. \tag{A53}$$

A.4.3. Indentation analysis

The indentation analysis for an insulating punch is quite similar to that for a conducting punch although there are some distinctions. Thus, a series of parallel results can be obtained. For an arbitrary axisymmetric and insulating indenter, the total load applied during the indentation is given by

$$\begin{aligned} p_1^{\mathrm{I}} &= -\tfrac{2ad}{\pi g_{11}} + \tfrac{2}{\pi g_{11}}\textstyle\int_0^a \sqrt{a^2-\rho^2}f'(\rho)\mathrm{d}\rho \\ &= -2a\sqrt{-\tfrac{2a\eta^*}{g_{11}}} - \tfrac{2}{\pi g_{11}}\textstyle\int_0^a \frac{\rho^2 f'(\rho)}{\sqrt{a^2-\rho^2}}\mathrm{d}\rho, \end{aligned} \tag{A54}$$

for which the following two relations have been employed

$$\chi_0(t) = \frac{1}{g_{11}}\left[d - t\int_0^t \frac{f'(\rho)\mathrm{d}\rho}{\sqrt{t^2-\rho^2}}\right], \tag{A55}$$

$$d = -\pi\sqrt{-2ag_{11}\eta^*} + \int_0^a \frac{af'(x)\mathrm{d}x}{\sqrt{a^2-x^2}}. \tag{A56}$$

With respect to the general profile of the indenter in Eq. (6), Eqs. (A54)–(A56) become

$$d = -\frac{\pi g_{11}}{2a}p_1^{\mathrm{I}} + \sqrt{\pi}\sum_{n=1}^{\infty}\frac{\Gamma(\frac{n}{2}+1)}{\Gamma(\frac{n+1}{2})}r_n a^n, \tag{A57}$$

$$\chi_0(a) = \frac{1}{g_{11}}(d - \sqrt{\pi}\sum_{n=1}^{\infty}\frac{\Gamma(\frac{n}{2}+1)}{\Gamma(\frac{n+1}{2})}r_n a^n), \tag{A58}$$

$$\begin{aligned} p_1^{\mathrm{I}} = &-\frac{2a}{\sqrt{\pi}g_{11}}\sum_{n=1}^{\infty}\frac{n\Gamma(\frac{n}{2}+1)}{(n+1)\Gamma(\frac{n+1}{2})}r_n a^n - 2a \\ &\times\sqrt{-\frac{2a}{g_{11}}\eta\sqrt{1+\left(\sum_{n=1}^{\infty}nr_n a^{n-1}\right)^2}}. \end{aligned} \tag{A59}$$

For smooth punches, the contact radius due to adhesion (a_0), can be similarly obtained from the following equation:

$$\left[\sum_{n=1}^{\infty}\frac{n\Gamma(\frac{n}{2}+1)}{(n+1)\Gamma(\frac{n+1}{2})}r_n a_0^n\right]^2 = -2\pi g_{11}\eta a_0\sqrt{1+\left(\sum_{n=1}^{\infty}nr_n a_0^{n-1}\right)^2}. \tag{A60}$$

Appendix B. Related parameters

B.1. Non-zero components of the effective material tensors

$$\begin{aligned}
\mathscr{A}_{01111} &= 2\lambda_3^{-1}\{\Omega_1 + \lambda_1^2[(2\Omega_{11}+\Omega_2) + 4\Omega_{12}\lambda_1^2 + 2\Omega_{22}\lambda_1^4] \\
&\quad +\Omega_2\lambda_3^2 + 2\lambda_1^2\lambda_3^2[2\Omega_{12} + 2(\Omega_{13}+\Omega_{22})\lambda_1^2 \\
&\quad +\Omega_3/2 + 2\Omega_{23}\lambda_1^4 + \Omega_{22}\lambda_3^2 + 2\Omega_{23}\lambda_1^2\lambda_3^2 + \Omega_{33}\lambda_1^4\lambda_3^2]\},
\end{aligned}$$

$$\begin{aligned}
\mathscr{A}_{01122} &= 4\lambda_1^2\lambda_3^{-1}[\Omega_{11} + \Omega_2 + 2\Omega_{12}\lambda_1^2 + \Omega_{22}\lambda_1^4 \ + (2\Omega_{12}+\Omega_3)\lambda_3^2 \\
&\quad +\Omega_{22}\lambda_3^4 + \lambda_1^2\lambda_3^2(2\Omega_{13} + 2\Omega_{22} \\
&\quad +2\Omega_{23}\lambda_1^2 + 2\Omega_{23}\lambda_3^2 + \Omega_{33}\lambda_1^2\lambda_3^2)],
\end{aligned}$$

$$\begin{aligned}
\mathscr{A}_{01133} &= 4\lambda_3[\Omega_{11} + \Omega_2 + (3\Omega_{12}+\Omega_3)\lambda_1^2 + (\Omega_{13}+2\Omega_{22})\lambda_1^4 + \Omega_{23}\lambda_1^6 \\
&\quad +\Omega_{12}\lambda_3^2 + (\Omega_{13}+2\Omega_{22})\lambda_1^2\lambda_3^2 + 3\Omega_{23}\lambda_1^4\lambda_3^2 + \Omega_{33}\lambda_1^6\lambda_3^2] \\
&\quad +4D_3^2\lambda_1^{-2}\lambda_3^{-1}\{\lambda_1^8\lambda_3^4(\Omega_{35}+2\Omega_{36}\lambda_3^2) \\
&\quad +\lambda_1^6\lambda_3^2[\Omega_{15} + 2\Omega_{16}\lambda_3^2 + (\Omega_{25}+2\Omega_{26}\lambda_3^2)(\lambda_1^2+\lambda_3^2)]\},
\end{aligned}$$

$$\begin{aligned}
\mathscr{A}_{03333} &= 2\lambda_3\lambda_1^{-2}\{\Omega_1 + 2\Omega_2\lambda_1^2 + \Omega_3\lambda_1^4 + 2\lambda_3^2[\Omega_{11} + 4\Omega_{12}\lambda_1^2 \\
&\quad +\lambda_1^4(2\Omega_{13} + 4\Omega_{22} + 4\Omega_{23}\lambda_1^2 + \Omega_{33}\lambda_1^4)]\} + 2D_3^2\lambda_1^{-2}\lambda_3^{-1}\{4\Omega_{35}\lambda_1^8\lambda_3^4 \\
&\quad +\lambda_3^2[8\Omega_{36}\lambda_1^8\lambda_3^4 + \Omega_5\lambda_1^4 + 2\lambda_1^4\lambda_3^2(2\Omega_{15} + 3\Omega_6 + 4\Omega_{25}\lambda_1^2 + 4\Omega_{16}\lambda_3^2 \\
&\quad +8\Omega_{26}\lambda_1^2\lambda_3^2)]\} + 4D_3^4\lambda_1^6\lambda_3^3[\Omega_{55} + 4\lambda_3^2(\Omega_{56}+\Omega_{66}\lambda_3^2)],
\end{aligned}$$

$$\mathscr{A}_{01212} = \frac{2}{\lambda_3}(\Omega_1 + \Omega_2\lambda_3^2),\ \mathscr{A}_{01221} = -\frac{2\lambda_1^2}{\lambda_3}(\Omega_2 + \Omega_3\lambda_3^2),$$

$$\begin{aligned}
\mathscr{A}_{01313} &= \frac{2}{\lambda_3}(\Omega_1 + \Omega_2\lambda_1^2 + D_3^2\Omega_6\lambda_1^4\lambda_3^2), \\
\mathscr{A}_{01331} &= -2\lambda_3(\Omega_2 + \Omega_3\lambda_1^2 - D_3^2\Omega_6\lambda_1^4), \\
\mathscr{A}_{03131} &= \frac{2\lambda_3}{\lambda_1^2}\{\Omega_1 + \Omega_2\lambda_1^2 + D_3^2\lambda_1^4[\Omega_5 + \Omega_6(\lambda_1^2+2\lambda_3^2)]\},
\end{aligned} \tag{B1}$$

$$\begin{aligned}
\Gamma_{0113} &= \tfrac{4D_3\lambda_1^4}{\lambda_3}\{\Omega_{14} + \Omega_{24}(\lambda_1^2+\lambda_3^2) + \lambda_3^2[\Omega_{15} + \Omega_{34}\lambda_1^2 + \Omega_{16}\lambda_3^2 \\
&\quad +(\Omega_{26}+\Omega_{35})\lambda_1^2\lambda_3^2 + \Omega_{26}\lambda_3^4 + \Omega_{36}\lambda_1^2\lambda_3^4 + \Omega_{25}(\lambda_1^2+\lambda_3^2)]\}, \\
\Gamma_{0131} &= 2D_3\lambda_1^2\lambda_3[\Omega_5 + \Omega_6(\lambda_1^2+\lambda_3^2)], \\
\Gamma_{0333} &= 4D_3\lambda_1^2\lambda_3\{\Omega_{14} + \Omega_5 + 2\Omega_{24}\lambda_1^2 + \Omega_{34}\lambda_1^4 \\
&\quad +(\Omega_{15}+2\Omega_6)\lambda_3^2 + \Omega_{16}\lambda_3^4 + \lambda_1^2\lambda_3^2(2\Omega_{25} + 2\Omega_{26}\lambda_3^2 + \Omega_{35}\lambda_1^2 \\
&\quad +\Omega_{36}\lambda_1^2\lambda_3^2) + D_3^2\lambda_1^4[\Omega_{45} + (2\Omega_{46}+\Omega_{55})\lambda_3^2 \\
&\quad +3\Omega_{56}\lambda_3^4 + 2\Omega_{66}\lambda_3^6]\},
\end{aligned} \tag{B2}$$

$$K_{011} = 2\lambda_3(\Omega_4 + \Omega_5\lambda_1^2 + \Omega_6\lambda_1^4),$$

$$\begin{aligned}
K_{033} &= 2\lambda_1^2\lambda_3^{-1}\{\Omega_4 + \lambda_3^2(\Omega_5 + \Omega_6\lambda_3^2) + 2D_3^2\lambda_1^4[\Omega_{44} + 2\Omega_{45}\lambda_3^2 \\
&\quad +\lambda_3^4(2\Omega_{46} + \Omega_{55} + 2\Omega_{56}\lambda_3^2 + \Omega_{66}\lambda_3^4)]\},
\end{aligned} \tag{B3}$$

where $\mathscr{A}_{01111} - \mathscr{A}_{01122} = \mathscr{A}_{01212} + \mathscr{A}_{01221}$.

B.2. Expressions of h_{ij}

$$\begin{cases}
h_{11} = \frac{-\gamma_{23}\varpi_{12}+\gamma_{22}\varpi_{13}}{2\pi(\gamma_{13}(\gamma_{22}\varpi_{11}-\gamma_{21}\varpi_{12})+\gamma_{12}(-\gamma_{23}\varpi_{11}+\gamma_{21}\varpi_{13})+\gamma_{11}(\gamma_{23}\varpi_{12}-\gamma_{22}\varpi_{13}))}, \\
h_{21} = \frac{\gamma_{23}\varpi_{11}-\gamma_{21}\varpi_{13}}{2\pi(\gamma_{13}(\gamma_{22}\varpi_{11}-\gamma_{21}\varpi_{12})+\gamma_{12}(-\gamma_{23}\varpi_{11}+\gamma_{21}\varpi_{13})+\gamma_{11}(\gamma_{23}\varpi_{12}-\gamma_{22}\varpi_{13}))}, \\
h_{31} = \frac{-\gamma_{22}\varpi_{11}+\gamma_{21}\varpi_{12}}{2\pi(\gamma_{13}(\gamma_{22}\varpi_{11}-\gamma_{21}\varpi_{12})+\gamma_{12}(-\gamma_{23}\varpi_{11}+\gamma_{21}\varpi_{13})+\gamma_{11}(\gamma_{23}\varpi_{12}-\gamma_{22}\varpi_{13}))},
\end{cases} \tag{B4}$$

$$\begin{cases}
h_{12} = \frac{\gamma_{13}\varpi_{12}-\gamma_{12}\varpi_{13}}{2\pi(\gamma_{13}(\gamma_{22}\varpi_{11}-\gamma_{21}\varpi_{12})+\gamma_{12}(-\gamma_{23}\varpi_{11}+\gamma_{21}\varpi_{13})+\gamma_{11}(\gamma_{23}\varpi_{12}-\gamma_{22}\varpi_{13}))}, \\
h_{22} = \frac{-\gamma_{13}\varpi_{11}+\gamma_{11}\varpi_{13}}{2\pi(\gamma_{13}(\gamma_{22}\varpi_{11}-\gamma_{21}\varpi_{12})+\gamma_{12}(-\gamma_{23}\varpi_{11}+\gamma_{21}\varpi_{13})+\gamma_{11}(\gamma_{23}\varpi_{12}-\gamma_{22}\varpi_{13}))}, \\
h_{32} = \frac{\gamma_{12}\varpi_{11}-\gamma_{11}\varpi_{12}}{2\pi(\gamma_{13}(\gamma_{22}\varpi_{11}-\gamma_{21}\varpi_{12})+\gamma_{12}(-\gamma_{23}\varpi_{11}+\gamma_{21}\varpi_{13})+\gamma_{11}(\gamma_{23}\varpi_{12}-\gamma_{22}\varpi_{13}))}.
\end{cases} \tag{B5}$$

Appendix C. Exact solutions for three typical indenters

Following Fabrikant (1989), Fabrikant (1991), we substitute Eq. (A22) into Eq. (A17) and obtain

$$H_j(\rho,\psi,z)=\frac{1}{\pi^2}\int_0^{2\pi}\int_0^a H(\rho,\psi,z;r_0,\phi_0)\omega_j(N_0)r_0\mathrm{d}r_0\mathrm{d}\phi_0, \tag{C1}$$

where

$$\begin{aligned}H(\rho,\psi,z;r_0,\phi_0)=&-R^{-1}(M,N_0)\tan^{-1}[hR^{-1}(M,N_0)]\\&+(a^2-r_0^2)^{-\frac{1}{2}}\ln[(a+\sqrt{a^2-l_1^2})l_1^{-1}]\\&+(a^2-r_0^2)^{-\frac{1}{2}}(\zeta-1)^{-\frac{1}{2}}\tan^{-1}[\sqrt{a^2-l_1^2}(\zeta-1)^{-\frac{1}{2}}a^{-1}]\\&+(a^2-r_0^2)^{-\frac{1}{2}}(\bar{\zeta}-1)^{-\frac{1}{2}}\tan^{-1}[\sqrt{a^2-l_1^2}(\bar{\zeta}-1)^{-\frac{1}{2}}a^{-1}],\end{aligned} \tag{C2}$$

and

$$\zeta=\frac{\rho}{\rho_0}e^{i(\psi-\phi_0)},\quad \bar{\zeta}=\frac{\rho}{\rho_0}e^{-i(\psi-\phi_0)}. \tag{C3}$$

The following simple notations are also adopted:

$$\begin{cases}l_1\triangleq l_1(\rho,a,z)=\frac{1}{2}\left[\sqrt{(\rho+a)^2+z^2}-\sqrt{(\rho-a)^2+z^2}\right],\\ l_2\triangleq l_2(\rho,a,z)=\frac{1}{2}\left[\sqrt{(\rho+a)^2+z^2}+\sqrt{(\rho-a)^2+z^2}\right],\\ l_{1i}=l_1(\rho,a,z_i),\\ l_{2i}=l_2(\rho,a,z_i)\end{cases} \tag{C4}$$

Then, the explicit expressions of 3D adhesive contact solutions for a soft electroactive half-space can be obtained, which are given below.

C.1. Circular flat-ended punch

(1) Conducting case:

$$\psi_i=\kappa_{1i}^{\mathrm{C}}\left[z_i\sin^{-1}\left(\frac{a}{l_{2i}}\right)-\sqrt{a^2-l_{1i}^2}+a\ln\left(l_{2i}+\sqrt{l_{2i}^2-\rho^2}\right)\right], \tag{C5}$$

where $\kappa_{1i}^{\mathrm{C}}=2\sqrt{\pi a}\sum_{j=1}^{2}h_{ij}K_j^{\mathrm{C}}$. Thus

$$\begin{aligned}&u_\rho=\sum_{i=1}^{3}\kappa_{1i}^{\mathrm{C}}\frac{a-\sqrt{a^2-l_{1i}^2}}{\rho},u_z=\sum_{i=1}^{3}\alpha_{1i}\kappa_{1i}^{\mathrm{C}}\sin^{-1}\left(\frac{a}{l_{2i}}\right),\\&\varphi=\sum_{i=1}^{3}a_{2i}\kappa_{1i}^{\mathrm{C}}\sin^{-1}\left(\frac{a}{l_{2i}}\right),\end{aligned} \tag{C6}$$

$$\begin{aligned}&\sigma_{z1}=\sum_{i=1}^{3}\gamma_{1i}\kappa_{1i}^{\mathrm{C}}\frac{\sqrt{a^2-l_{1i}^2}}{l_{1i}^2-l_{2i}^2},\sigma_{z2}=\sum_{i=1}^{3}\gamma_{2i}\kappa_{1i}^{\mathrm{C}}\frac{\sqrt{a^2-l_{1i}^2}}{l_{1i}^2-l_{2i}^2},\\&\sigma_{z3}=\sum_{i=1}^{3}\gamma_{3i}\kappa_{1i}^{\mathrm{C}}\frac{\sqrt{a^2-l_{1i}^2}}{l_{1i}^2-l_{2i}^2},\end{aligned} \tag{C7}$$

$$\begin{aligned}&\sigma_{\rho1}=\sum_{i=1}^{3}\varpi_{1i}\kappa_{1i}^{\mathrm{C}}\frac{l_{1i}\sqrt{\rho^2-l_{1i}^2}}{\rho\left(l_{1i}^2-l_{2i}^2\right)},\sigma_{\rho2}=\sum_{i=1}^{3}\varpi_{2i}\kappa_{1i}^{\mathrm{C}}\frac{l_{1i}\sqrt{\rho^2-l_{1i}^2}}{\rho\left(l_{1i}^2-l_{2i}^2\right)},\\&\sigma_{\rho3}=\sum_{i=1}^{3}\varpi_{3i}\kappa_{1i}^{\mathrm{C}}\frac{l_{1i}\sqrt{\rho^2-l_{1i}^2}}{\rho\left(l_{1i}^2-l_{2i}^2\right)}.\end{aligned} \tag{C8}$$

(2) Insulating case:

$$\psi_i=\kappa_{1i}^{\mathrm{I}}\left[z_i\sin^{-1}\left(\frac{a}{l_{2i}}\right)-\sqrt{a^2-l_{1i}^2}+a\ln\left(l_{2i}+\sqrt{l_{2i}^2-\rho^2}\right)\right], \tag{C9}$$

where $\kappa_{1i}^{\mathrm{I}}=2\sqrt{\pi a}h_{i1}K_{i1}^{\mathrm{I}}$. Thus

$$\begin{aligned}&u_\rho=\sum_{i=1}^{3}\kappa_{1i}^{\mathrm{I}}\frac{a-\sqrt{a^2-l_{1i}^2}}{\rho},u_z=\sum_{i=1}^{3}\alpha_{1i}\kappa_{1i}^{\mathrm{I}}\sin^{-1}\left(\frac{a}{l_{2i}}\right),\\&\varphi=\sum_{i=1}^{3}a_{2i}\kappa_{1i}^{\mathrm{I}}\sin^{-1}\left(\frac{a}{l_{2i}}\right),\end{aligned} \tag{C10}$$

$$\begin{aligned}&\sigma_{z1}=\sum_{i=1}^{3}\gamma_{1i}\kappa_{1i}^{\mathrm{I}}\frac{\sqrt{a^2-l_{1i}^2}}{l_{1i}^2-l_{2i}^2},\sigma_{z2}=\sum_{i=1}^{3}\gamma_{2i}\kappa_{1i}^{\mathrm{I}}\frac{\sqrt{a^2-l_{1i}^2}}{l_{1i}^2-l_{2i}^2},\\&\sigma_{z3}=\sum_{i=1}^{3}\gamma_{3i}\kappa_{1i}^{\mathrm{I}}\frac{\sqrt{a^2-l_{1i}^2}}{l_{1i}^2-l_{2i}^2},\end{aligned} \tag{C11}$$

$$\begin{aligned}&\sigma_{\rho1}=\sum_{i=1}^{3}\varpi_{1i}\kappa_{1i}^{\mathrm{I}}\frac{l_{1i}\sqrt{\rho^2-l_{1i}^2}}{\rho\left(l_{1i}^2-l_{2i}^2\right)},\sigma_{\rho2}=\sum_{i=1}^{3}\varpi_{2i}\kappa_{1i}^{\mathrm{I}}\frac{l_{1i}\sqrt{\rho^2-l_{1i}^2}}{\rho\left(l_{1i}^2-l_{2i}^2\right)},\\&\sigma_{\rho3}=\sum_{i=1}^{3}\varpi_{3i}\kappa_{1i}^{\mathrm{I}}\frac{l_{1i}\sqrt{\rho^2-l_{1i}^2}}{\rho\left(l_{1i}^2-l_{2i}^2\right)}.\end{aligned} \tag{C12}$$

C.2. Conical punch

(1) Conducting case:

$$\begin{aligned}\psi_i=&\kappa_{2i}^{\mathrm{C1}}[z_i\sin^{-1}(\tfrac{a}{l_{2i}})-\sqrt{a^2-l_{1i}^2}+a\ln(l_{2i}+\sqrt{l_{2i}^2-\rho^2})]\\&+\kappa_{2i}^{\mathrm{C2}}[az_i\sin^{-1}(\tfrac{a}{l_{2i}})+\tfrac{1}{4}(2a^2+\rho^2-2z_i^2)\ln(l_{2i}+\sqrt{l_{2i}^2-\rho^2})\\&-\tfrac{3}{4}z_i\sqrt{\rho^2+z_i^2}+\tfrac{3l_{2i}(\rho^2-2l_{1i}^2)\sqrt{a^2-l_{1i}^2}}{4\rho l_{1i}}\\&-\tfrac{\rho^2-2z_i^2}{4}\ln(z_i+\sqrt{\rho^2+z_i^2})],\end{aligned} \tag{C13}$$

where $\kappa_{2i}^{\mathrm{C1}}=2\sqrt{\pi a}\sum_{j=1}^{2}h_{ij}K_j^{\mathrm{C}}$ and $\kappa_{2i}^{\mathrm{C2}}=\sum_{j=1}^{2}h_{ij}T_j^{\mathrm{C}}$, with $T_1^{\mathrm{C}}=g_{22}\cot\beta/A_0$, and $T_2^{\mathrm{C}}=-(g_{21}/g_{22})T_1^{\mathrm{C}}$. Thus

$$\begin{aligned}u_\rho=&\sum_{i=1}^{3}\kappa_{2i}^{\mathrm{C1}}\tfrac{a-\sqrt{a^2-l_{1i}^2}}{\rho}+\kappa_{2i}^{\mathrm{C2}}[-\tfrac{z_i\sqrt{\rho^2+z_i^2}}{2\rho}+\tfrac{(\rho l_{2i}-2al_{1i})\sqrt{l_{2i}^2-\rho^2}}{2\rho^2}+\tfrac{a^2}{2\rho}\\&-\tfrac{\rho}{2}\ln(z_i+\sqrt{\rho^2+z_i^2})+\tfrac{\rho}{2}\ln(l_{2i}+\sqrt{l_{2i}^2-\rho^2})],\\u_z=&\sum_{i=1}^{3}\alpha_{1i}\{\kappa_{2i}^{\mathrm{C1}}\sin^{-1}\left(\tfrac{a}{l_{2i}}\right)+\kappa_{2i}^{\mathrm{C2}}[\sqrt{l_{2i}^2-a^2}-\sqrt{\rho^2+z_i^2}+a\sin^{-1}(\tfrac{a}{l_{2i}})\\&+z_i\ln(z_i+\sqrt{\rho^2+z_i^2})-z_i\ln(l_{2i}+\sqrt{l_{2i}^2-\rho^2})]\},\\\varphi=&\sum_{i=1}^{3}\alpha_{2i}\{\kappa_{2i}^{\mathrm{C1}}\sin^{-1}\left(\tfrac{a}{l_{2i}}\right)+\kappa_{2i}^{\mathrm{C2}}[\sqrt{l_{2i}^2-a^2}-\sqrt{\rho^2+z_i^2}+a\sin^{-1}(\tfrac{a}{l_{2i}})\\&+z_i\ln(z_i+\sqrt{\rho^2+z_i^2})-z_i\ln(l_{2i}+\sqrt{l_{2i}^2-\rho^2})]\},\end{aligned} \tag{C14}$$

$$\begin{aligned}\sigma_{z1}=&\sum_{i=1}^{3}\gamma_{1i}\{\kappa_{2i}^{\mathrm{C1}}\tfrac{\sqrt{a^2-l_{1i}^2}}{l_{1i}^2-l_{2i}^2}-\kappa_{2i}^{\mathrm{C2}}[\ln(l_{2i}+\sqrt{l_{2i}^2-\rho^2})-\ln(z_i+\sqrt{\rho^2+z_i^2})]\},\\\sigma_{z2}=&\sum_{i=1}^{3}\gamma_{2i}\{\kappa_{2i}^{\mathrm{C1}}\tfrac{\sqrt{a^2-l_{1i}^2}}{l_{1i}^2-l_{2i}^2}-\kappa_{2i}^{\mathrm{C2}}[\ln(l_{2i}+\sqrt{l_{2i}^2-\rho^2})-\ln(z_i+\sqrt{\rho^2+z_i^2})]\},\\\sigma_{z3}=&\sum_{i=1}^{3}\gamma_{3i}\{\kappa_{2i}^{\mathrm{C1}}\tfrac{\sqrt{a^2-l_{1i}^2}}{l_{1i}^2-l_{2i}^2}-\kappa_{2i}^{\mathrm{C2}}[\ln(l_{2i}+\sqrt{l_{2i}^2-\rho^2})-\ln(z_i+\sqrt{\rho^2+z_i^2})]\},\end{aligned} \tag{C15}$$

$$\sigma_{\rho 1}=\sum_{i=1}^{3}\varpi_{1i}[\kappa_{2i}^{C1}\frac{l_{1i}\sqrt{\rho^2-l_{1i}^2}}{\rho(l_{1i}^2-l_{2i}^2)}+\kappa_{2i}^{C2}\frac{\sqrt{l_{2i}^2-a^2}-\sqrt{\rho^2+z_i^2}}{\rho}],$$
$$\sigma_{\rho 2}=\sum_{i=1}^{3}\varpi_{2i}[\kappa_{2i}^{C1}\frac{l_{1i}\sqrt{\rho^2-l_{1i}^2}}{\rho(l_{1i}^2-l_{2i}^2)}+\kappa_{2i}^{C2}\frac{\sqrt{l_{2i}^2-a^2}-\sqrt{\rho^2+z_i^2}}{\rho}],\tag{C16}$$
$$\sigma_{\rho 3}=\sum_{i=1}^{3}\varpi_{3i}[\kappa_{2i}^{C1}\frac{l_{1i}\sqrt{\rho^2-l_{1i}^2}}{\rho(l_{1i}^2-l_{2i}^2)}+\kappa_{2i}^{C2}\frac{\sqrt{l_{2i}^2-a^2}-\sqrt{\rho^2+z_i^2}}{\rho}].$$

(2) Insulating case:

$$\begin{aligned}\psi_i&=\kappa_{2i}^{I1}[z_i\sin^{-1}(\tfrac{a}{l_{2i}})-\sqrt{a^2-l_{1i}^2}+a\ln(l_{2i}+\sqrt{l_{2i}^2-\rho^2})]\\&+\kappa_{2i}^{I2}[az_i\sin^{-1}(\tfrac{a}{l_{2i}})+\tfrac{1}{4}(2a^2+\rho^2-2z_i^2)\ln(l_{2i}+\sqrt{l_{2i}^2-\rho^2})\\&-\tfrac{3}{4}z_i\sqrt{\rho^2+z_i^2}+\tfrac{3l_{2i}(\rho^2-2l_{1i}^2)\sqrt{a^2-l_{1i}^2}}{4\rho l_{1i}}\\&-\tfrac{\rho^2-2z_i^2}{4}\ln(z_i+\sqrt{\rho^2+z_i^2})],\end{aligned}\tag{C17}$$

where $\kappa_{2i}^{I1}=2\sqrt{\pi a}h_{i1}K_1^I$ and $\kappa_{2i}^{I2}=h_{i1}T_1^I$, with $T_1^I=\cot\beta/g_{11}$. Thus

$$\begin{aligned}u_\rho&=\sum_{i=1}^{3}\kappa_{2i}^{I1}\tfrac{a-\sqrt{a^2-l_{1i}^2}}{\rho}+\kappa_{2i}^{I2}[-\tfrac{z_i\sqrt{\rho^2+z_i^2}}{2\rho}+\tfrac{(\rho l_{2i}-2al_{1i})\sqrt{l_{2i}^2-\rho^2}}{2\rho^2}+\tfrac{a^2}{2\rho}\\&-\tfrac{\rho}{2}\ln(z_i+\sqrt{\rho^2+z_i^2})+\tfrac{\rho}{2}\ln(l_{2i}+\sqrt{l_{2i}^2-\rho^2})],\\u_z&=\sum_{i=1}^{3}\alpha_{1i}\{\kappa_{2i}^{I1}\sin^{-1}\left(\tfrac{a}{l_{2i}}\right)+\kappa_{2i}^{I2}[\sqrt{l_{2i}^2-a^2}-\sqrt{\rho^2+z_i^2}+a\sin^{-1}(\tfrac{a}{l_{2i}})\\&+z_i\ln(z_i+\sqrt{\rho^2+z_i^2})-z_i\ln(l_{2i}+\sqrt{l_{2i}^2-\rho^2})]\},\\\varphi&=\sum_{i=1}^{3}\alpha_{2i}\{\kappa_{2i}^{I1}\sin^{-1}\left(\tfrac{a}{l_{2i}}\right)+\kappa_{2i}^{I2}[\sqrt{l_{2i}^2-a^2}-\sqrt{\rho^2+z_i^2}+a\sin^{-1}(\tfrac{a}{l_{2i}})\\&+z_i\ln(z_i+\sqrt{\rho^2+z_i^2})-z_i\ln(l_{2i}+\sqrt{l_{2i}^2-\rho^2})]\},\end{aligned}\tag{C18}$$

$$\begin{aligned}\sigma_{z1}&=\sum_{i=1}^{3}\gamma_{1i}\{\kappa_{2i}^{I1}\tfrac{\sqrt{a^2-l_{1i}^2}}{l_{1i}^2-l_{2i}^2}-\kappa_{2i}^{I2}[\ln(l_{2i}+\sqrt{l_{2i}^2-\rho^2})-\ln(z_i+\sqrt{\rho^2+z_i^2})]\},\\\sigma_{z2}&=\sum_{i=1}^{3}\gamma_{2i}\{\kappa_{2i}^{I1}\tfrac{\sqrt{a^2-l_{1i}^2}}{l_{1i}^2-l_{2i}^2}-\kappa_{2i}^{I2}[\ln(l_{2i}+\sqrt{l_{2i}^2-\rho^2})-\ln(z_i+\sqrt{\rho^2+z_i^2})]\},\\\sigma_{z3}&=\sum_{i=1}^{3}\gamma_{3i}\{\kappa_{2i}^{I1}\tfrac{\sqrt{a^2-l_{1i}^2}}{l_{1i}^2-l_{2i}^2}-\kappa_{2i}^{I2}[\ln(l_{2i}+\sqrt{l_{2i}^2-\rho^2})-\ln(z_i+\sqrt{\rho^2+z_i^2})]\},\end{aligned}\tag{C19}$$

$$\begin{aligned}\sigma_{\rho 1}&=\sum_{i=1}^{3}\varpi_{1i}[\kappa_{2i}^{I1}\tfrac{l_{1i}\sqrt{\rho^2-l_{1i}^2}}{\rho(l_{1i}^2-l_{2i}^2)}+\kappa_{2i}^{I2}\tfrac{\sqrt{l_{2i}^2-a^2}-\sqrt{\rho^2+z_i^2}}{\rho}],\\\sigma_{\rho 2}&=\sum_{i=1}^{3}\varpi_{2i}[\kappa_{2i}^{I1}\tfrac{l_{1i}\sqrt{\rho^2-l_{1i}^2}}{\rho(l_{1i}^2-l_{2i}^2)}+\kappa_{2i}^{I2}\tfrac{\sqrt{l_{2i}^2-a^2}-\sqrt{\rho^2+z_i^2}}{\rho}],\\\sigma_{\rho 3}&=\sum_{i=1}^{3}\varpi_{3i}[\kappa_{2i}^{I1}\tfrac{l_{1i}\sqrt{\rho^2-l_{1i}^2}}{\rho(l_{1i}^2-l_{2i}^2)}+\kappa_{2i}^{I2}\tfrac{\sqrt{l_{2i}^2-a^2}-\sqrt{\rho^2+z_i^2}}{\rho}].\end{aligned}\tag{C20}$$

C.3. Spherical punch

(1) Conducting case:

$$\begin{aligned}\psi_i&=\kappa_{3i}^{C1}[z_i\sin^{-1}(\tfrac{a}{l_{2i}})-\sqrt{a^2-l_{1i}^2}+a\ln(l_{2i}+\sqrt{l_{2i}^2-\rho^2})]\\&+\kappa_{3i}^{C2}[z_i(2a^2-\rho^2+\tfrac{2}{3}z_i^2)\sin^{-1}(\tfrac{a}{l_{2i}})+\tfrac{4}{3}a^3\ln(l_{2i}+\sqrt{l_{2i}^2-\rho^2})\\&+\tfrac{1}{3}(5\rho^2-\tfrac{10}{3}a^2-2l_{2i}^2-\tfrac{11}{3}l_{1i}^2)\sqrt{a^2-l_{1i}^2}],\end{aligned}\tag{C21}$$

where $\kappa_{3i}^{C1}=2\sqrt{\pi a}\sum_{j=1}^{2}h_{ij}K_j^C$ and $\kappa_{3i}^{C2}=\sum_{j=1}^{2}h_{ij}T_j^C$, with $T_1^C=g_{22}/(\pi RA_0)$ and $T_2^C=-(g_{21}/g_{22})T_1^C$. Thus

$$\begin{aligned}u_\rho&=\sum_{i=1}^{3}\kappa_{3i}^{C1}\tfrac{a-\sqrt{a^2-l_{1i}^2}}{\rho}+2\kappa_{3i}^{C2}\rho[\sqrt{a^2-l_{1i}^2}\left(1-\tfrac{l_{1i}^2+2a^2}{3\rho^2}\right)\\&+\tfrac{2a^3}{3\rho^2}-z_i\sin^{-1}\left(\tfrac{a}{l_{2i}}\right)],\\u_z&=\sum_{i=1}^{3}\alpha_{1i}\{\kappa_{3i}^{C1}\sin^{-1}\left(\tfrac{a}{l_{2i}}\right)+\kappa_{3i}^{C2}[(2a^2+2z_i^2-\rho^2)\sin^{-1}\left(\tfrac{a}{l_{2i}}\right)\\&-\tfrac{2a^2-3l_{1i}^2}{a}\sqrt{l_{2i}^2-a^2}]\},\\\varphi&=\sum_{i=1}^{3}\alpha_{2i}\{\kappa_{3i}^{C1}\sin^{-1}\left(\tfrac{a}{l_{2i}}\right)+\kappa_{3i}^{C2}[(2a^2+2z_i^2-\rho^2)\sin^{-1}\left(\tfrac{a}{l_{2i}}\right)\\&-\tfrac{2a^2-3l_{1i}^2}{a}\sqrt{l_{2i}^2-a^2}]\}.\end{aligned}\tag{C22}$$

$$\begin{aligned}\sigma_{z1}&=\sum_{i=1}^{3}\gamma_{1i}\{\kappa_{3i}^{C1}\tfrac{\sqrt{a^2-l_{1i}^2}}{l_{1i}^2-l_{2i}^2}+4\kappa_{3i}^{C2}[z_i\sin^{-1}\left(\tfrac{a}{l_{2i}}\right)-\sqrt{a^2-l_{1i}^2}]\},\\\sigma_{z2}&=\sum_{i=1}^{3}\gamma_{2i}\{\kappa_{3i}^{C1}\tfrac{\sqrt{a^2-l_{1i}^2}}{l_{1i}^2-l_{2i}^2}+4\kappa_{3i}^{C2}[z_i\sin^{-1}\left(\tfrac{a}{l_{2i}}\right)-\sqrt{a^2-l_{1i}^2}]\},\\\sigma_{z3}&=\sum_{i=1}^{3}\gamma_{3i}\{\kappa_{3i}^{C1}\tfrac{\sqrt{a^2-l_{1i}^2}}{l_{1i}^2-l_{2i}^2}+4\kappa_{3i}^{C2}[z_i\sin^{-1}\left(\tfrac{a}{l_{2i}}\right)-\sqrt{a^2-l_{1i}^2}]\},\end{aligned}\tag{C23}$$

$$\begin{aligned}\sigma_{\rho 1}&=\sum_{i=1}^{3}\varpi_{1i}\{\kappa_{3i}^{C1}\tfrac{l_{1i}\sqrt{\rho^2-l_{1i}^2}}{\rho(l_{1i}^2-l_{2i}^2)}+2\kappa_{3i}^{C2}\rho[\tfrac{a}{l_{2i}^2}\sqrt{l_{2i}^2-a^2}-\sin^{-1}\left(\tfrac{a}{l_{2i}}\right)]\},\\\sigma_{\rho 2}&=\sum_{i=1}^{3}\varpi_{2i}\{\kappa_{3i}^{C1}\tfrac{l_{1i}\sqrt{\rho^2-l_{1i}^2}}{\rho(l_{1i}^2-l_{2i}^2)}+2\kappa_{3i}^{C2}\rho[\tfrac{a}{l_{2i}^2}\sqrt{l_{2i}^2-a^2}-\sin^{-1}\left(\tfrac{a}{l_{2i}}\right)]\},\\\sigma_{\rho 3}&=\sum_{i=1}^{3}\varpi_{3i}\{\kappa_{3i}^{C1}\tfrac{l_{1i}\sqrt{\rho^2-l_{1i}^2}}{\rho(l_{1i}^2-l_{2i}^2)}+2\kappa_{3i}^{C2}\rho[\tfrac{a}{l_{2i}^2}\sqrt{l_{2i}^2-a^2}-\sin^{-1}\left(\tfrac{a}{l_{2i}}\right)]\}.\end{aligned}\tag{C24}$$

(2) Insulating case:

$$\begin{aligned}\psi_i&=\kappa_{3i}^{I1}[z_i\sin^{-1}(\tfrac{a}{l_{2i}})-\sqrt{a^2-l_{1i}^2}+a\ln(l_{2i}+\sqrt{l_{2i}^2-\rho^2})]\\&+\kappa_{3i}^{I2}[z_i(2a^2-\rho^2+\tfrac{2}{3}z_i^2)\sin^{-1}(\tfrac{a}{l_{2i}})+\tfrac{4}{3}a^3\ln(l_{2i}+\sqrt{l_{2i}^2-\rho^2})\\&+\tfrac{1}{3}(5\rho^2-\tfrac{10}{3}a^2-2l_{2i}^2-\tfrac{11}{3}l_{1i}^2)\sqrt{a^2-l_{1i}^2}],\end{aligned}\tag{C25}$$

where $\kappa_{3i}^{I1}=2\sqrt{\pi a}h_{i1}K_1^I$ and $\kappa_{3i}^{I2}=h_{i1}T_1^I$, with $T_1^I=1/(\pi Rg_{11})$. Thus

$$\begin{aligned}u_\rho&=\sum_{i=1}^{3}\kappa_{3i}^{I1}\tfrac{a-\sqrt{a^2-l_{1i}^2}}{\rho}+2\kappa_{3i}^{I2}\rho[\sqrt{a^2-l_{1i}^2}\left(1-\tfrac{l_{1i}^2+2a^2}{3\rho^2}\right)\\&+\tfrac{2a^3}{3\rho^2}-z_i\sin^{-1}\left(\tfrac{a}{l_{2i}}\right)],\\u_z&=\sum_{i=1}^{3}\alpha_{1i}\{\kappa_{3i}^{I1}\sin^{-1}\left(\tfrac{a}{l_{2i}}\right)+\kappa_{3i}^{I2}[(2a^2+2z_i^2-\rho^2)\sin^{-1}\left(\tfrac{a}{l_{2i}}\right)\\&-\tfrac{2a^2-3l_{1i}^2}{a}\sqrt{l_{2i}^2-a^2}]\},\\\varphi&=\sum_{i=1}^{3}\alpha_{2i}\{\kappa_{3i}^{I1}\sin^{-1}\left(\tfrac{a}{l_{2i}}\right)+\kappa_{3i}^{I2}[(2a^2+2z_i^2-\rho^2)\sin^{-1}\left(\tfrac{a}{l_{2i}}\right)\\&-\tfrac{2a^2-3l_{1i}^2}{a}\sqrt{l_{2i}^2-a^2}]\},\end{aligned}\tag{C26}$$

$$\begin{aligned}\sigma_{z1}&=\sum_{i=1}^{3}\gamma_{1i}\{\kappa_{3i}^{I1}\tfrac{\sqrt{a^2-l_{1i}^2}}{l_{1i}^2-l_{2i}^2}+4\kappa_{3i}^{I2}[z_i\sin^{-1}\left(\tfrac{a}{l_{2i}}\right)-\sqrt{a^2-l_{1i}^2}]\},\\\sigma_{z2}&=\sum_{i=1}^{3}\gamma_{2i}\{\kappa_{3i}^{I1}\tfrac{\sqrt{a^2-l_{1i}^2}}{l_{1i}^2-l_{2i}^2}+4\kappa_{3i}^{I2}[z_i\sin^{-1}\left(\tfrac{a}{l_{2i}}\right)-\sqrt{a^2-l_{1i}^2}]\},\\\sigma_{z3}&=\sum_{i=1}^{3}\gamma_{3i}\{\kappa_{3i}^{I1}\tfrac{\sqrt{a^2-l_{1i}^2}}{l_{1i}^2-l_{2i}^2}+4\kappa_{3i}^{I2}[z_i\sin^{-1}\left(\tfrac{a}{l_{2i}}\right)-\sqrt{a^2-l_{1i}^2}]\},\end{aligned}\tag{C27}$$

$$\sigma_{\rho 1}=\sum_{i=1}^{3}\varpi_{1i}\{\kappa_{3i}^{l1}\frac{l_{1i}\sqrt{\rho^2-l_{1i}^2}}{\rho\left(l_{1i}^2-l_{2i}^2\right)}+2\kappa_{3i}^{l2}\rho[\frac{a}{l_{2i}^2}\sqrt{l_{2i}^2-a^2}-\sin^{-1}\left(\frac{a}{l_{2i}}\right)]\},$$
$$\sigma_{\rho 2}=\sum_{i=1}^{3}\varpi_{2i}\{\kappa_{3i}^{l1}\frac{l_{1i}\sqrt{\rho^2-l_{1i}^2}}{\rho\left(l_{1i}^2-l_{2i}^2\right)}+2\kappa_{3i}^{l2}\rho[\frac{a}{l_{2i}^2}\sqrt{l_{2i}^2-a^2}-\sin^{-1}\left(\frac{a}{l_{2i}}\right)]\},$$
$$\sigma_{\rho 3}=\sum_{i=1}^{3}\varpi_{3i}\{\kappa_{3i}^{l1}\frac{l_{1i}\sqrt{\rho^2-l_{1i}^2}}{\rho\left(l_{1i}^2-l_{2i}^2\right)}+2\kappa_{3i}^{l2}\rho[\frac{a}{l_{2i}^2}\sqrt{l_{2i}^2-a^2}-\sin^{-1}\left(\frac{a}{l_{2i}}\right)]\}. \tag{C28}$$

Appendix D. Surface instability of a half-space

We investigate the surface instability of a pre-deformed half-space by following Dorfmann and Ogden (2010a). We look for incremental two-dimensional solutions such that

$$(u_1,u_3)=(\mathrm{i}A,B)\mathrm{e}^{-\bar{k}sx_3}\mathrm{e}^{\mathrm{i}\bar{k}x_1},\quad u_2=0,\ \varphi=C\mathrm{e}^{-\bar{k}sx_3}\mathrm{e}^{\mathrm{i}\bar{k}x_1}, \tag{D1}$$

where $\bar{k}$ is the positive 'wavenumber' of disturbance and $Re(s)>0$ is required to satisfy the decay condition at infinity. Then, substitution of Eq. (D1) into the incremental governing equations leads to

$$\begin{cases}(s^2c_{88}-c_{11})A-s(c_{13}+c_{58})B-s(e_{15}+e_{31})C=0,\\ s(c_{13}+c_{58})A+(c_{33}s^2-c_{55})B+(e_{33}s^2-e_{15})C=0,\\ s(e_{15}+e_{31})A+(e_{33}s^2-e_{15})B-(\varepsilon_{33}s^2-\varepsilon_{11})C=0,\end{cases} \tag{D2}$$

whose determinant must vanish for non-trivial solutions to exist. Thus, Eq. (D1) is transformed, with the zero component omitted, into

$$(u_1,u_3)=\sum_{i=1}^{3}(\mathrm{i}A_i,B_i)\mathrm{e}^{-\bar{k}s_ix_3}\mathrm{e}^{\mathrm{i}\bar{k}x_1},$$
$$\varphi=\sum_{i=1}^{3}C_i\mathrm{e}^{-\bar{k}s_ix_3}\mathrm{e}^{\mathrm{i}\bar{k}x_1}, \tag{D3}$$

where the constants A_i, B_i and C_i are connected by any two equations of Eq. (D2) such as

$$\begin{cases}(s_i^2c_{88}-c_{11})A_i-s_i(c_{13}+c_{58})B_i-s_i(e_{15}+e_{31})C_i=0,\\ s_i(c_{13}+c_{58})A_i+(c_{33}s_i^2-c_{55})B_i+(e_{33}s_i^2-e_{15})C_i=0,\end{cases} \tag{D4}$$

where there is no summation over i.

The mechanical boundary conditions of Eq. $(4)_1$ specialize to

$$\dot{T}_{031}=0,\dot{T}_{033}=0. \tag{D5}$$

By using Eq. (D3), we rewrite Eq. (D5) into

$$\begin{cases}\sum_{i=1}^{3}-s_ic_{88}A_i+c_{58}B_i+e_{15}C_i=0,\\ \sum_{i=1}^{3}c_{13}A_i+s_ic_{33}B_i+s_ie_{33}C_i=0.\end{cases} \tag{D6}$$

Correspondingly, the electric boundary conditions in Eqs. $(4)_2$ and $(4)_3$ reduce to

$$\dot{D}_{l03}=0,\dot{E}_{l01}=0. \tag{D7}$$

and, equivalently, to

$$\sum_{i=1}^{3}e_{31}A_i+s_ie_{33}B_i-s_i\varepsilon_{33}C_i=0,\sum_{i=1}^{3}C_i=0, \tag{D8}$$

at $x_3=0$.

In this paper, we carefully distinguish these two cases, which correspond to the prescribed surface free charge (q) and the prescribed electric potential (φ), respectively. To obtain non-trivial solutions, the determinant of coefficients satisfies the following bifurcation equation:

$$\begin{vmatrix}A_{11}&0&0&A_{14}&0&0&A_{17}&0&0\\0&A_{22}&0&0&A_{25}&0&0&A_{28}&0\\0&0&A_{33}&0&0&A_{36}&0&0&A_{39}\\A_{41}&0&0&A_{44}&0&0&A_{47}&0&0\\0&A_{52}&0&0&A_{55}&0&0&A_{58}&0\\0&0&A_{63}&0&0&A_{66}&0&0&A_{69}\\A_{71}&A_{72}&A_{73}&A_{74}&A_{75}&A_{76}&A_{77}&A_{78}&A_{79}\\A_{81}&A_{82}&A_{83}&A_{84}&A_{85}&A_{86}&A_{87}&A_{88}&A_{89}\\A_{91}&A_{92}&A_{93}&A_{94}&A_{95}&A_{96}&A_{97}&A_{98}&A_{99}\end{vmatrix}=0, \tag{D9}$$

where $(i=1,\ 2,\ 3)$

$$A_{ii}=s_i^2c_{88}-c_{11},\ A_{i(i+3)}=-s_i(c_{13}+c_{58}),\ A_{i(i+6)}=-s_i(e_{15}+e_{31}),$$
$$A_{(i+3)i}=s_i(c_{13}+c_{58}),\ A_{(i+3)(i+3)}=s_i^2c_{33}-c_{55},\ A_{(i+3)(i+6)}=e_{33}s_i^2-e_{15}, \tag{D10}$$

$$A_{7i}=-s_ic_{88},\qquad A_{7(i+3)}=c_{58},\qquad A_{7(i+6)}=e_{15},$$
$$A_{8i}=c_{13},\qquad A_{8(i+3)}=s_ic_{33},\qquad A_{8(i+6)}=s_ie_{33}, \tag{D11}$$

and

$$A_{9i}=e_{31},\qquad A_{9(i+3)}=s_ie_{33},\qquad A_{9(i+6)}=-s_i\varepsilon_{33}, \tag{D12}$$

for $\dot{D}_{l03}=0$, while

$$A_{9i}=A_{9(i+3)}=0,\qquad A_{9(i+6)}=1, \tag{D13}$$

for $\dot{E}_{l01}=0$.

Appendix E. Corresponding results for a perfectly insulating flat-ended indenter

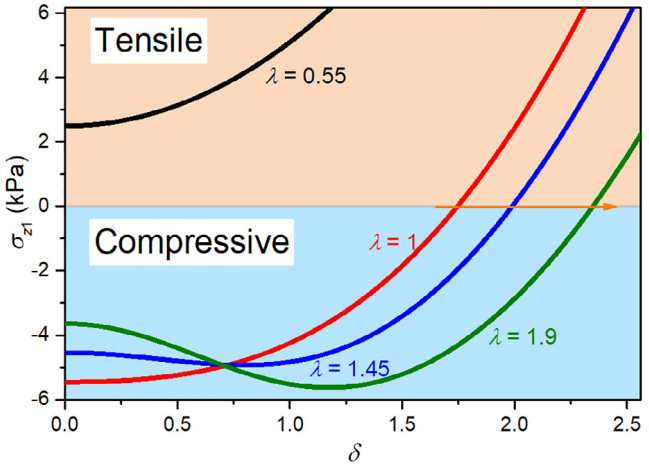

Fig. E1. Variations with the dimensionless electric displacement δ of the incremental normal stress at the center of the contact region under a perfectly insulating flat-ended punch.

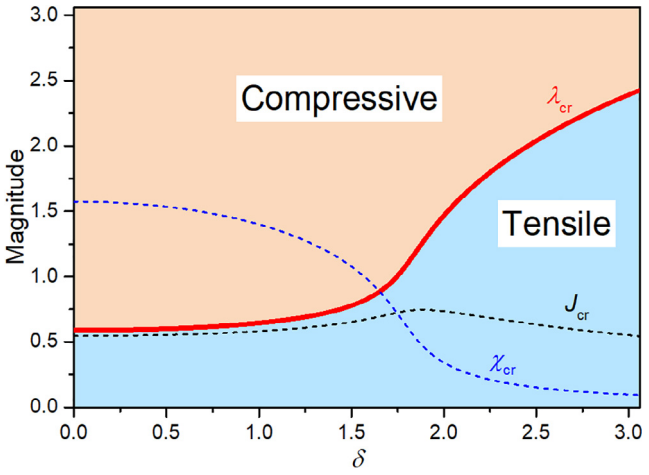

Fig. E2. Variations with the dimensionless electric displacement of the critical prestretch and volume ratio corresponding to zero incremental normal stress at the center of the contact area under a perfectly insulating flat-ended punch.

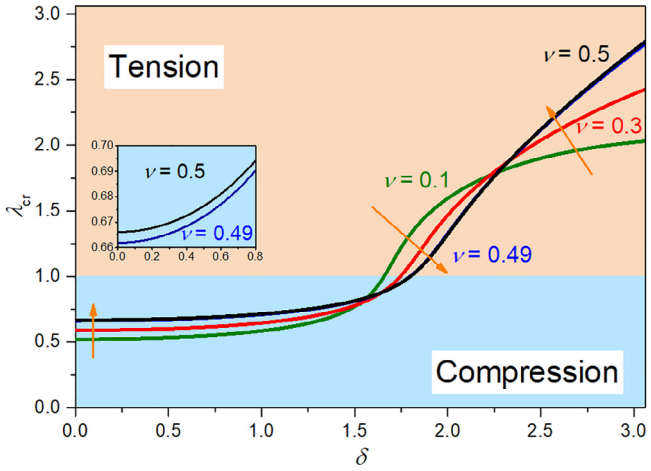

Fig. E3. Variations of the critical stretch λ_{cr} with the dimensionless electric displacement δ for an SEA half-space under a perfectly insulating flat-ended punch for $\varepsilon = 1$ and various values of ν.

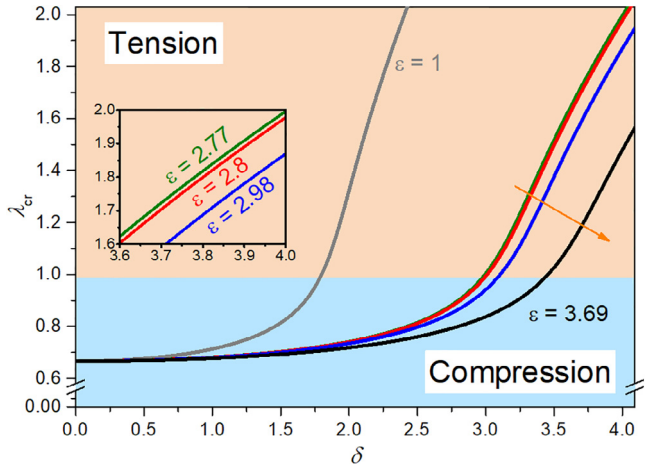

Fig. E4. Variations of the critical stretch λ_{cr} with the dimensionless electric displacement δ for an SEA half-space under a perfectly insulating flat-ended circular punch for various values of ε.

Appendix F

Supplementary results for the validity analysis of linear theory.

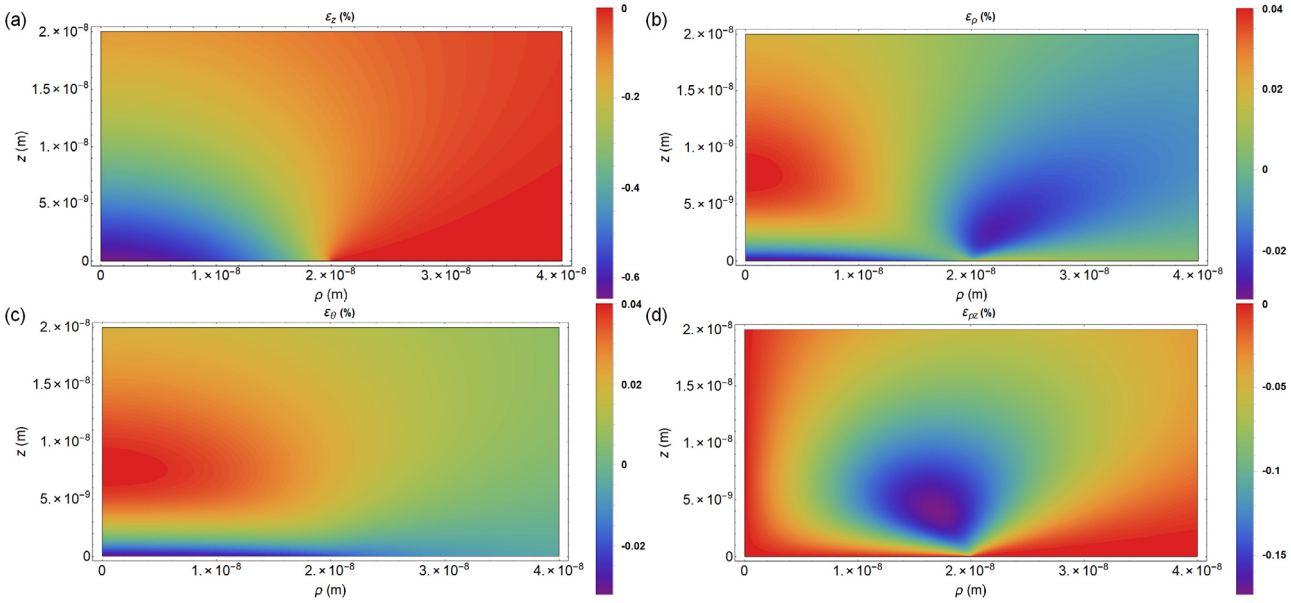

Fig. F1. Three-dimensional distributions of all the nonzero incremental strains for an SEA half-space under a perfectly conducting spherical punch (R = 4 μm, d = 0.1 nm) with nearly zero dimensionless electric displacement (δ = 0.00001) and no adhesion: (a) incremental normal strain (ε_z); (b) incremental radial strain (ε_ρ); (c) incremental circumferential strain (ε_θ); (d) incremental shearing strain ($\varepsilon_{\rho z}$). Note that the contact radius in this case is 20 nm.

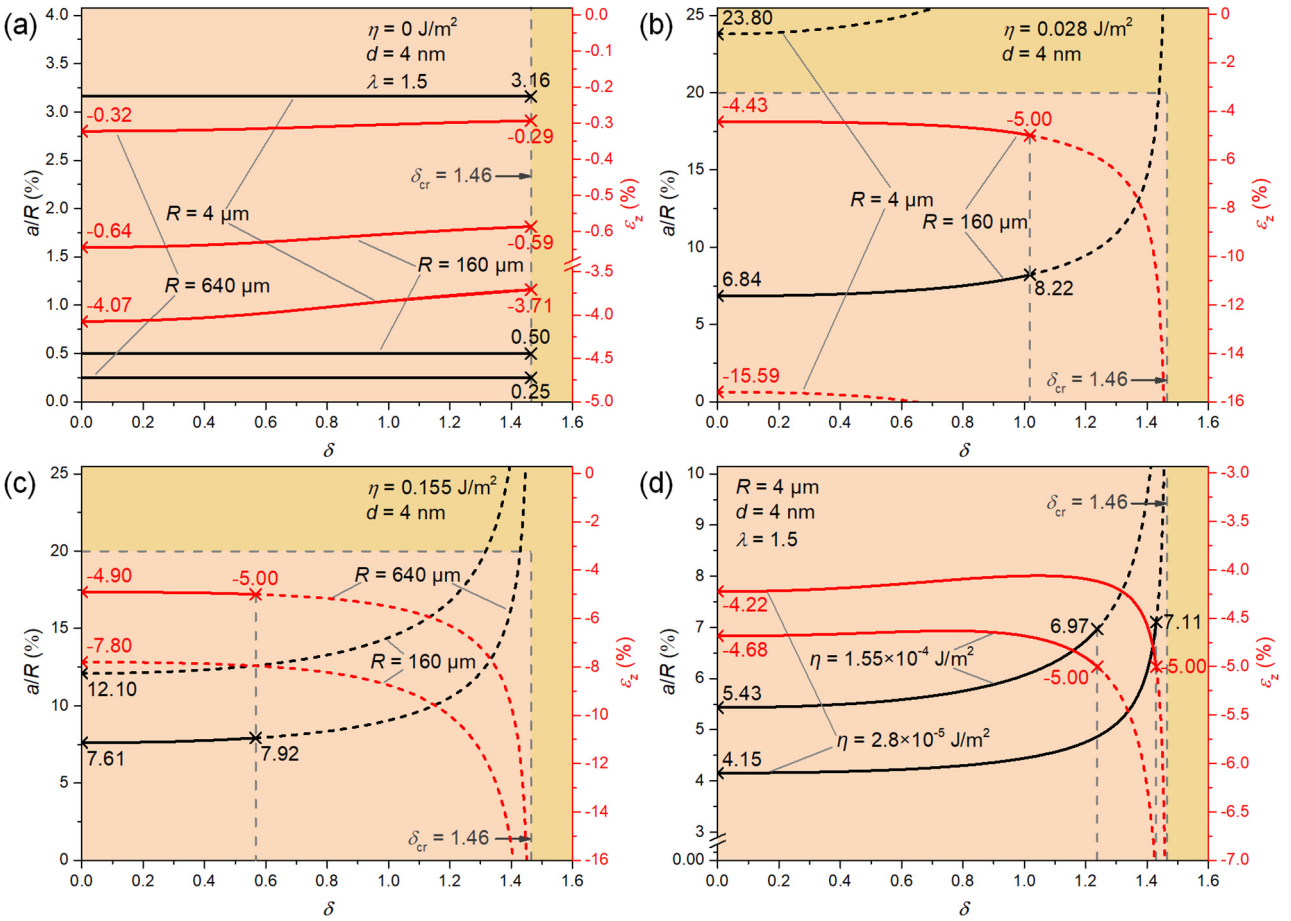

Fig. F2. Variations of the dimensionless contact radius (a/R) and the incremental normal strain at the center of contact area (ε_z) with the dimensionless electric displacement (δ) for an SEA half-space under a perfectly conducting spherical punch of different sizes (R = 4, 160, 640 μm) for various values of surface adhesion energy per unit area: (a) Adhesion-free (η = 0 J/m^2); (b) η = 0.028 J/m^2; (c) η = 0.155 J/m^2; (d) effects of the dimensionless electric biasing field and the weak adhesion on the dimensionless contact radius when the radius of the indenter and the indentation depth are 4 μm and 4 nm respectively.

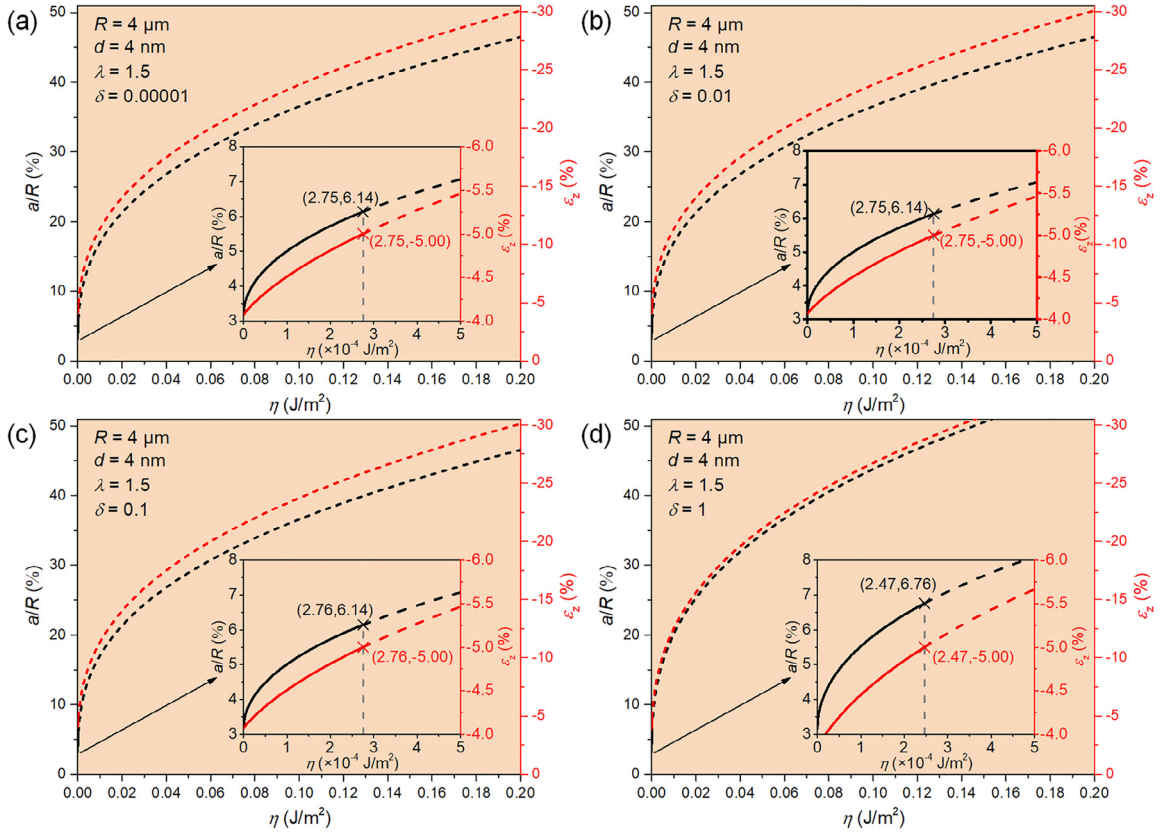

Fig. F3. Variations of the dimensionless contact radius (a/R) and the incremental normal strain (ε_z) with the adhesion energy per unit area (η) for a pre-stretched SEA half-space (λ = 1.5) under a perfectly conducting spherical punch of radius 4 μm when the indentation depth is 4 nm: (a) δ = 0.00001; (b) δ = 0.01; (c) δ = 0.1; (d) δ = 1.

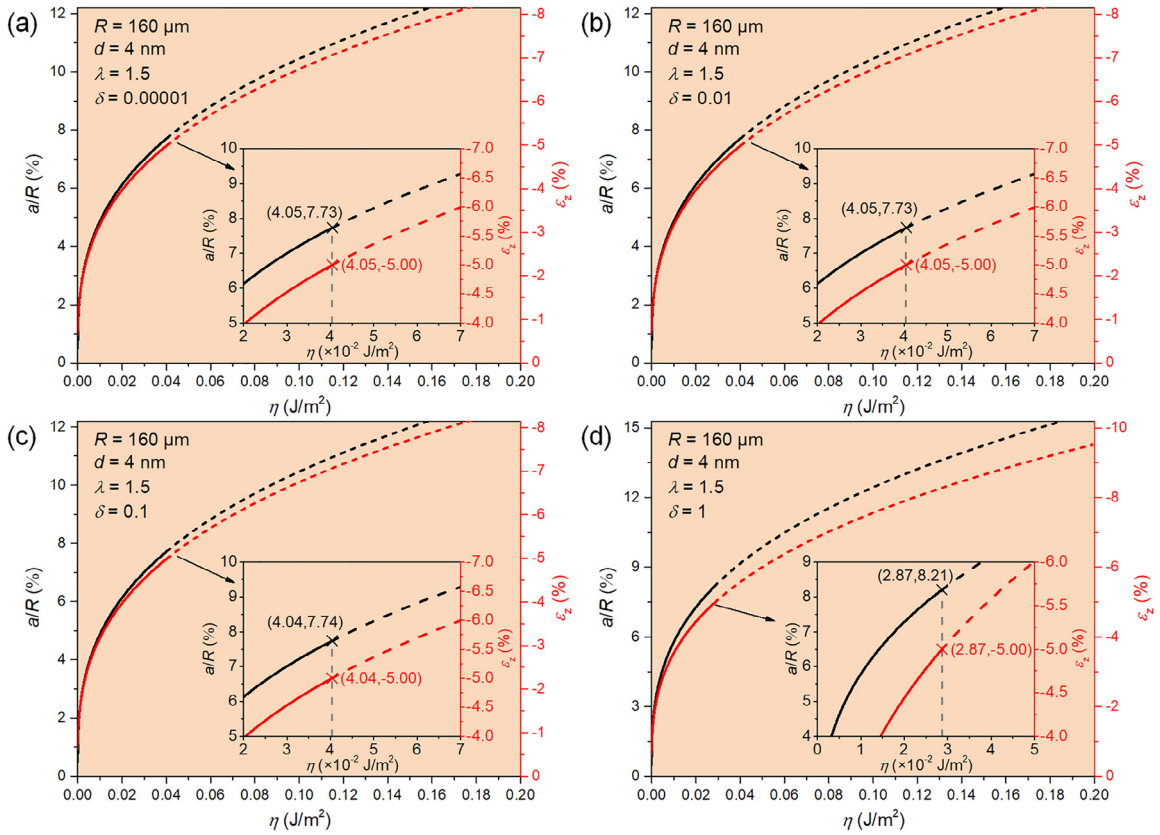

Fig. F4. Variations of the dimensionless contact radius (a/R) and the incremental normal strain (ε_z) with the adhesion energy per unit area (η) for a pre-stretched SEA half-space (λ = 1.5) under a perfectly conducting spherical punch of radius 160 μm when the indentation depth is 4 nm: (a) δ = 0.00001; (b) δ = 0.01; (c) δ = 0.1; (d) δ = 1.

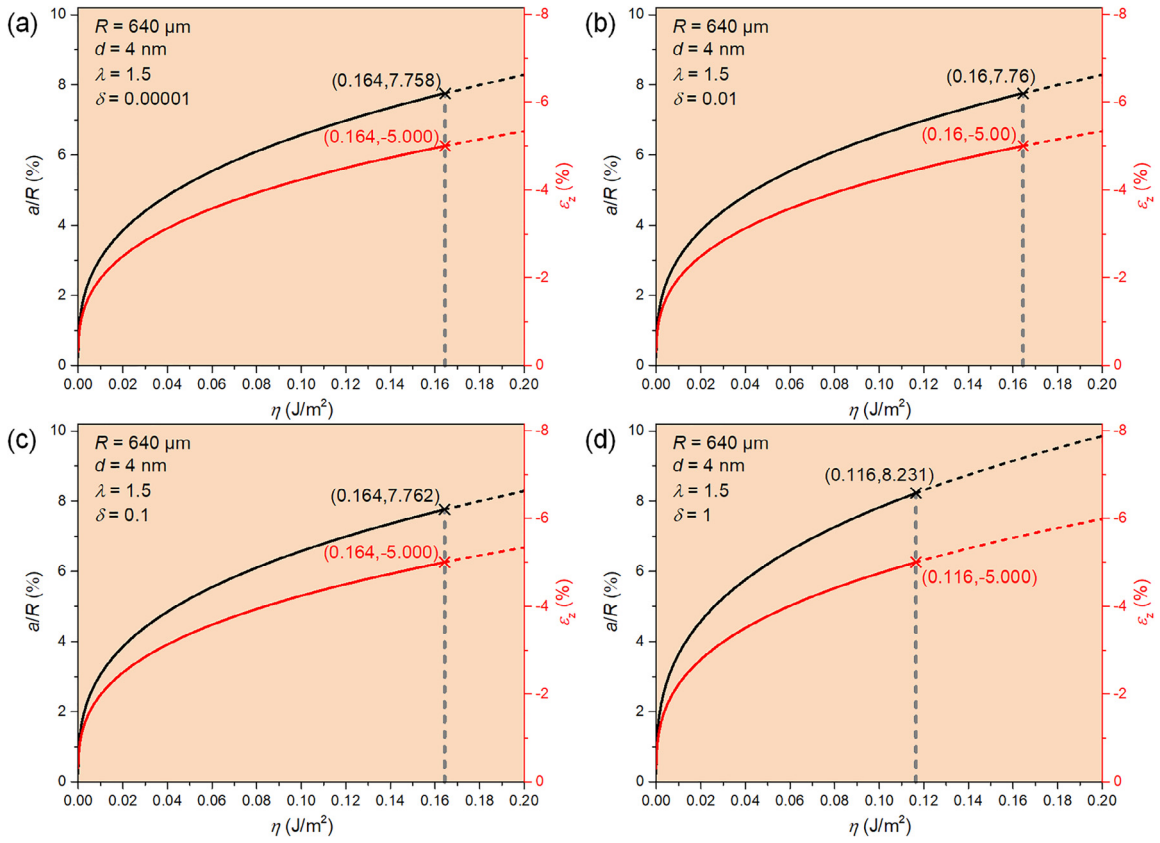

Fig. F5. Variations of the dimensionless contact radius (a/R) and the incremental normal strain (ε_z) with the adhesion energy per unit area (η) for a pre-stretched SEA half-space (λ = 1.5) under a perfectly conducting spherical punch of radius 640 μm when the indentation depth is 640 nm: (a) δ = 0.00001; (b) δ = 0.01; (c) δ = 0.1; (d) δ = 1.

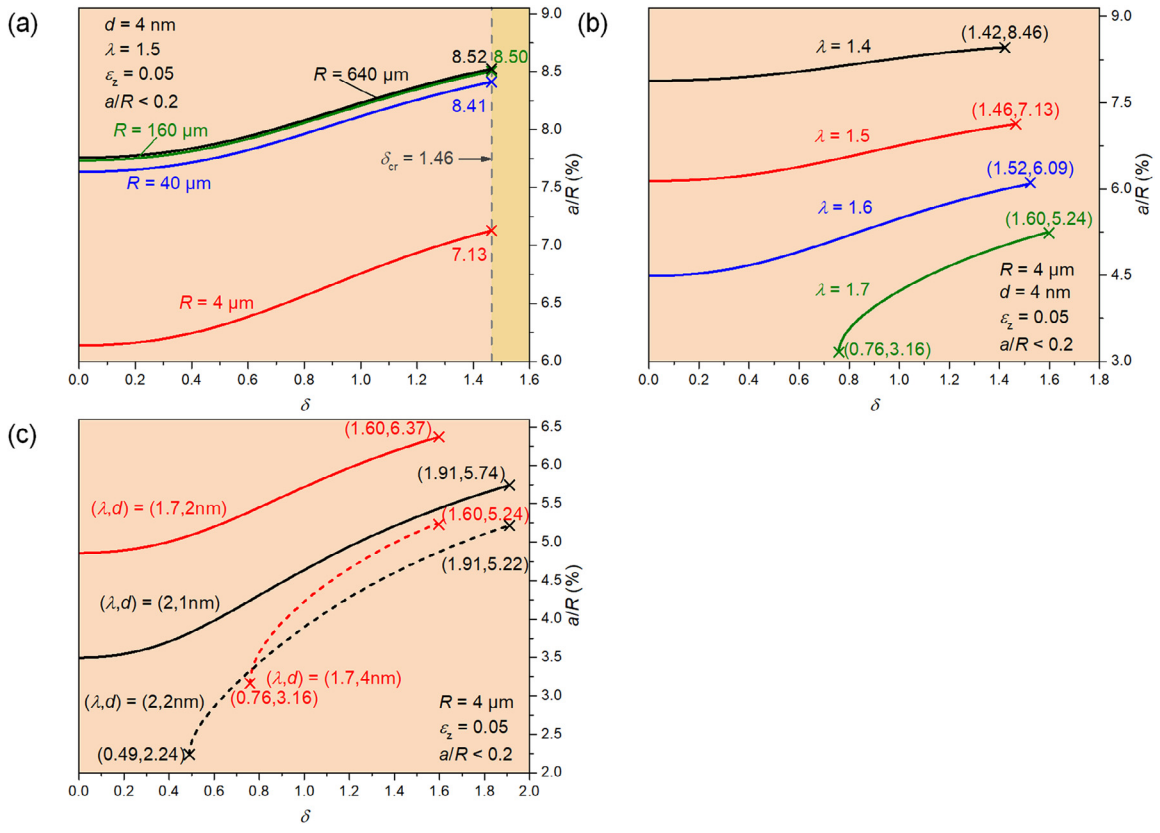

Fig. F6. Variations of a/R for the contact between an SEA half-space and a perfectly conducting and grounded spherical indenter for varying testing conditions and initial pre-stretch (λ): (a) different radii of indenters (R = 4, 40, 160, 640 μm) with fixed indentation depth (d = 4 nm) and pre-stretch (λ = 1.5); (b) different pre-stretches (λ = 1.4, 1.5, 1.6, 1.7) with fixed indentation depth (d = 4 nm) and radius of indenter (R = 4 μm); (c) different indentation depths (d = 1, 2, 4 nm) and pre-stretches (λ = 1.7, 2) with fixed indenter size (R = 4 μm).

References

Akbari, S., Rosset, S., Shea, H.R., 2013. Improved electromechanical behavior in castable dielectric elastomer actuators. Appl. Phys. Lett. 102, (7) 071906.

Arora, S., Ghosh, T., Muth, J., 2007. Dielectric elastomer based prototype fiber actuators. Sens. Actuators A Phys. 136 (1), 321–328.

Azzez, K., Chaabane, M., Abellan, M.-A., Bergheau, J.-M., Zahouani, H., Dogui, A., 2018. Relevance of indentation test to characterize soft biological tissue: application to human skin. Int. J. Appl. Mech. 10 (7), 1850074.

Bar-Cohen, Y. (Ed.), 2004. Electroactive Polymer (EAP) Actuators as Artificial Muscles: Reality, Potential, and Challenges. second ed. SPIE press, Bellingham.

Bauer, S., Bauer-Gogonea, S., Graz, I., Kaltenbrunner, M., Keplinger, C., Schwödiauer, R., 2014. 25th anniversary article: a soft future: from robots and sensor skin to energy harvesters. Adv. Mater. 26 (1), 149–162.

Beatty, M.F., Usmani, S.A., 1975. On the indentation of a highly elastic half-space. Q. J. Mech. Appl. Math. 28 (1), 47–62.

Bonilla, M.R., Stokes, J.R., Gidley, M.J., Yakubov, G.E., 2015. Interpreting atomic force microscopy nanoindentation of hierarchical biological materials using multi-regime analysis. Soft Matter 11 (7), 1281–1292.

Brochu, P., Pei, Q., 2010. Advances in dielectric elastomers for actuators and artificial muscles. Macromol. Rapid Commun. 31 (1), 10–36.

Calabri, L., Pugno, N., Menozzi, C., Valeri, S., 2008. AFM nanoindentation: tip shape and tip radius of curvature effect on the hardness measurement. J. Phys. Condens. Matter 20, 474208.

Cao, Y., Yang, D., Soboyejoy, W., 2005. Nanoindentation method for determining the initial contact and adhesion characteristics of soft polydimethylsiloxane. J. Mater. Res. 20 (8), 2004–2011.

Carpi, F., De Rossi, D., 2004. Dielectric elastomer cylindrical actuators: electromechanical modelling and experimental evaluation. Mater. Sci. Eng. C 24 (4), 555–562.

Carpi, F., De Rossi, D., Kornbluh, R., Pelrine, R.E., Sommer-Larsen, P., 2008a. Dielectric Elastomers as Electromechanical Transducers: Fundamentals, Materials, Devices, Models and Applications of an Emerging Electroactive Polymer Technology. Elsevier, Amsterdam.

Carpi, F., Gallone, G., Galantini, F., De Rossi, D., 2008b. Siliconepoly(hexylthiophene) blends as elastomers with enhanced electromechanical transduction properties. Adv. Funct. Mater. 18, 235–241.

Chen, W.Q., 2000. On piezoelastic contact problem for a smooth punch. Int. J. Solids Struct. 37 (16), 2331–2340.

Chen, W.Q., 2009. Adhesive contact between a rigid punch and a piezoelectric half-space. In: Yang, W., Feng, X.Q., Qin, Q.H. (Eds.), Advances in Damage, Fracture and Nanomechanics. Tsinghua University Press, Beijing, pp. 58–65 (in Chinese).

Chen, W.Q., 2015. Some recent advances in 3D crack and contact analysis of elastic solids with transverse isotropy and multi-field coupling. Acta Mech. Sin. 31 (5), 601–626.

Chen, W.Q., Ding, H.J., 1999. Indentation of a transversely isotropic piezoelectric half-space by a rigid sphere. Acta Mech. Solida Sin. 12 (2), 114–120.

Chen, W.Q., Ding, H.J., 2004. Potential theory method for 3D crack and contact problems of multi-field coupled media: a survey. J. Zhejiang Univ. (Science) 5 (9), 1009–1021.

Chen, W.Q., Pan, E.N., Wang, H.M., Zhang, C.Z., 2010. Theory of indentation on multiferroic composite materials. J. Mech. Phys. Solids 58 (10), 1524–1551.

Chen, W.Q., Shioya, T., Ding, H.J., 1999. The elasto-electric field for a rigid conical punch on a transversely isotropic piezoelectric half-space. J. Appl. Mech. 66 (3), 764–771.

Chen, Z.R., Yu, S.W., 2005. Micro-scale adhesive contact of a spherical rigid punch on a piezoelectric half-space. Comp. Sci. Tech. 65 (9), 1372–1381.

Choi, Y., Van Vliet, K.J., Li, J., Suresh, S., 2003. Size effects on the onset of plastic deformation during nanoindentation of thin films and patterned lines. J. Appl. Phys. 94 (9), 6050–6058.

Dagro, A.M., Ramesh, K.T., 2019. Nonlinear contact mechanics for the indentation of hyperelastic cylindrical bodies. Mech. Soft Mater. 1, 7.

Derjaguin, B.V., Muller, V.M., Toporov, Y.P., 1975. Effect of contact deformations on the adhesion of particles. J. Colloid Interface Sci. 53 (2), 314–326.

Ding, H.J., Chen, W.Q., Zhang, L.C., 2006. Elasticity of Transversely Isotropic Materials. Springer, Dordrecht.

Dorfmann, A., Ogden, R.W., 2010a. Electroelastic waves in a finitely deformed electroactive material. IMA J. Appl. Math. 75 (4), 603–636.

Dorfmann, A., Ogden, R.W., 2010b. Nonlinear electroelastostatics: Incremental equations and stability. Int. J. Eng. Sci. 48 (1), 1–14.

Dorfmann, L., Ogden, R.W., 2014. Instabilities of an electroelastic plate. Int. J. Eng. Sci. 77, 79–101.

Dos Santos Ferreira, O., Gelinck, E., de Graaf, D., Fischer, H., 2010. Adhesion experiments using an AFM—Parameters of influence. Appl. Surf. Sci. 257 (1), 48–55.

Ebenstein, D.M., Pruitt, L.A., 2006. Nanoindentation of biological materials. Nano Today 1 (3), 26–33.

Ericksen, J.L., 2007. Theory of elastic dielectrics revisited. Arch. Rational Mech. Anal. 183 (2), 299–313.

Fabrikant, V.I., 1989. Applications of Potential Theory in Mechanics: A Selection of New Results. Kluwer Academic Publishers, Dordrecht, Boston.

Fabrikant, V.I., 1991. Mixed Boundary Value Problems of Potential Theory and Their Applications in Engineering. Kluwer Academic Publishers, Dordrecht, Boston.

Getz, R., Kochmann, D.M., Shmuel, G., 2017. Voltage-controlled complete stopbands in two-dimensional soft dielectrics. Int. J. Solids Struct. 113, 24–36.

Giannakopoulos, A.E., Suresh, S., 1999. Theory of indentation of piezoelectric materials. Acta Mater. 47 (7), 2153–2164.

Green, A.E., Rivlin, R.S., Shield, R.T., Goldsbrough, G.R., 1952. General theory of small elastic deformations superposed on finite elastic deformations. Proc. R. Soc. Lond. A 211 (1104), 128–154.

Green, A.E., Zerna, W., 1954. Theoretical Elasticity. University Press, Oxford.

Gupta, S., Carrillo, F., Li, C., Pruitt, L., Puttlitz, C., 2007. Adhesive forces significantly affect elastic modulus determination of soft polymeric materials in nanoindentation. Mater. Lett. 61 (2), 448–451.

Hertz, H.R., 1881. Über die Berührung fester elastischer Körper. J. Reine. Angew. Math. 92, 156–171.

Huang, Y.L., Xia, G.Z., Zhou, W.J., Chen, W.Q., 2016. On the Green's functions for a two-phase soft electroactive medium subjected to biasing fields. Eng. Anal. Bound. Elem. 64, 137–149.

Johnson, K.L., Kendall, K., Roberts, A.D., 1971. Surface energy and the contact of elastic solids. Proc. R. Soc. Lond. A 324, 301–313.

Kalinin, S.V., Karapetian, E., Kachanov, M., 2004. Nanoelectromechanics of piezoresponse force microscopy. Phys. Rev. B 70, (18) 184101.

Kalinin, S.V., Rodriguez, B.J., Jesse, S., Karapetian, E., Mirman, B., Eliseev, E.A., Morozovska, A.N., 2007. Nanoscale electromechanics of ferroelectric and biological systems: a new dimension in scanning probe microscopy. Annu. Rev. Mater. Res. 37 (1), 189–238.

Karapetian, E., Kachanov, M., Kalinin, S.V., 2005. Nanoelectromechanics of piezoelectric indentation and applications to scanning probe microscopies of ferroelectric materials. Phil. Mag. 85 (10), 1017–1051.

Karapetian, E., Kachanov, M., Kalinin, S.V., 2009. Stiffness relations for piezoelectric indentation of flat and non-flat punches of arbitrary planform: applications to probing nanoelectromechanical properties of materials. J. Mech. Phys. Solids 57 (4), 673–688.

Karpitschka, S., van Wijngaarden, L., Snoeijer, J.H., 2016. Surface tension regularizes the crack singularity of adhesion. Soft Matter 12 (19), 4463–4471.

Kofod, G., Sommer-Larsen, P., Kornbluh, R., Pelrine, R., 2003. Actuation response of polyacrylate dielectric elastomers. J. Intell. Mater. Syst. Struct. 14 (12), 787–793.

Kolluru, P.V., Eaton, M.D., Collinson, D.W., Cheng, X., Delgado, D.E., Shull, K.R., Brinson, L.C., 2018. AFM-based dynamic scanning indentation (DSI) method for fast, high-resolution spatial mapping of local viscoelastic properties in soft materials. Macromol. 51 (21), 8964–8978.

Lei, H., Cheng, N., Zhao, J., 2018. Interaction between membrane and organic compounds studied by atomic force microscopy with a tip modification. J. Membrane Sci. 556, 178–184.

Li, J., Li, J.-F., Yu, Q., Chen, Q.N., Xie, S., 2015. Strain-based scanning probe microscopies for functional materials, biological structures, and electrochemical systems. J. Materiomics 1 (1), 3–21.

Li, J., Liu, L., Liu, Y., Leng, J., 2019. Dielectric elastomer spring-roll bending actuators: applications in soft robotics and design. Soft Robotics 6 (1), 69–81.

Li, Q.S., Lee, G.Y.H., Ong, C.N., Lim, C.T., 2008. AFM indentation study of breast cancer cells. Biochem. Biophys. Res. Commun. 374, 609–613.

Lin, D.C., Horkay, F., 2008. Nanomechanics of polymer gels and biological tissues: A critical review of analytical approaches in the Hertzian regime and beyond. Soft Matter 4, 669–682.

Linnebach, P., Simone, F., Rizzello, G., Seelecke, S., 2019. Development, manufacturing, and validation of a dielectric elastomer membrane actuator–driven contactor. J. Intell. Mater. Syst. Struct. 30 (4), 636–648.

Liu, Y., Zhang, Y., Chow, M.-J., Chen, Q.N., Li, J., 2012. Biological ferroelectricity uncovered in aortic walls by piezoresponse force microscopy. Phys. Rev. Lett. 108, (7) 078103.

Löwe, C., Zhang, X., Kovacs, G., 2005. Dielectric elastomers in actuator technology. Adv. Eng. Mater. 7 (5), 361–367.

Lu, P., Foo, Y.L., Shen, L., Cheong, D.W.C., O'Shea, S.J., 2011. A general relation for contact stiffness including adhesion in indentation analysis. J. Mater. Res. 26 (11), 1406–1413.

Luria, J., Kutes, Y., Moore, A., Zhang, L.H., Stach, E.A., Huey, B.D., 2016. Charge transport in CdTe solar cells revealed by conductive tomographic atomic force microscopy. Nat. Energy 1 (11), 16150.

Mark, J.E., 2009. Polymer Data Handbook. Oxford University Press, New York.

Maugis, D., 1992. Adhesion of spheres: the JKR-DMT transition using a Dugdale model. J. Colloid Interface Sci. 150 (1), 243–269.

Maugis, D., 2000. Contact. Contact, Adhesion and Rupture of Elastic Solids. Springer-Verlag, Berlin.

McKay, T.G., O'Brien, B.M., Calius, E.P., Anderson, I.A., 2011. Soft generators using dielectric elastomers. Appl. Phys. Lett. 98, (14) 142903.

Michałowski, M., Łuczak, S., 2018. AFM cantilevers with spherical tip of millimeter size. J. Micromech. Microeng. 29, 017002.

Mirfakhrai, T., Madden, J.D.W., Baughman, R.H., 2007. Polymer artificial muscles. Mater. Today 10 (4), 30–38.

Mirvakili, S.M., Hunter, I.W., 2018. Artificial muscles: mechanisms, applications, and challenges. Adv. Mater. 30 (6), 1704407.

Molberg, M., Crespy, D., Rupper, P., Nuesch, F., Manson, J.-A.-E., Lowe, C., Opris, D.M., 2010. High breakdown field dielectric elastomer actuators using encapsulated polyaniline as high dielectric constant filler. Adv. Funct. Mater. 20, 3280–3291.

Nowinski, J.L., 1969. Surface instability of a half-space under high two-dimensional compression. J. Franklin Inst. 288, 367–376.

O'Halloran, A., O'Malley, F., McHugh, P., 2008. A review on dielectric elastomer actuators, technology, applications, and challenges. J. Appl. Phys. 104, (7) 071101.

Oliver, W.C., Pharr, G.M., 1992. An improved technique for determining hardness and elastic modulus using load and displacement sensing indentation experiments. J. Mater. Res. 7 (6), 1564–1583.
Osmani, B., Seifi, S., Park, H.S., Leung, V., Töpper, T., Müller, B., 2017. Nanomechanical probing of thin-film dielectric elastomer transducers. Appl. Phys. Lett. 111, (9) 093104.
Pan, K., Liu, Y.Y., Xie, S.H., Liu, Y.M., Li, J.Y., 2013. The electromechanics of piezoresponse force microscopy for a transversely isotropic piezoelectric medium. Acta Mater. 61 (18), 7020–7033.
Pelrine, R., Kornbluh, R., Pei, Q., Joseph, J., 2000. High-speed electrically actuated elastomers with strain greater than 100%. Science 287 (5454), 836–839.
Pelrine, R.E., Kornbluh, R.D., Joseph, J.P., 1998. Electrostriction of polymer dielectrics with compliant electrodes as a means of actuation. Sens. Actuators A 64 (1), 77–85.
Racles, C., Dascalu, M., Bele, A., Tiron, V., Asandulesa, M., Tugui, C., Vasiliu, A.-L., Cazacu, M., 2017. All-silicone elastic composites with counter-intuitive piezoelectric response, designed for electromechanical applications. J. Mater. Chem. C 5 (28), 6997–7010.
Rizzello, G., Naso, D., York, A., Seelecke, S., 2016. Closed loop control of dielectric elastomer actuators based on self-sensing displacement feedback. Smart Mater. Struct. 25, (3) 035034.
Saha, R., Nix, W.D., 2002. Effects of the substrate on the determination of thin film mechanical properties by nanoindentation. Acta Mater. 50 (1), 23–38.
Schwarz, U.D., 2003. A generalized analytical model for the elastic deformation of an adhesive contact between a sphere and a flat surface. J. Colloid Interface Sci. 261 (1), 99–106.
Shankar, R., Ghosh, T.K., Spontak, R.J., 2007. Dielectric elastomers as next-generation polymeric actuators. Soft Matter 3 (9), 1116–1129.
Shian, S., Diebold, R.M., Clarke, D.R., 2013. Tunable lenses using transparent dielectric elastomer actuators. Opt. Express 21 (7), 8669–8676.
Su, Y.P., Broderick, H.C., Chen, W.Q., Destrade, M., 2018. Wrinkles in soft dielectric plates. J. Mech. Phys. Solids 119, 298–318.
Su, Y.P., Chen, W.Q., Destrade, M., 2019. Tuning the pull-in instability of soft dielectric elastomers through loading protocols. Int. J. Non-Linear Mech. 113, 62–66.
Suo, Z.G., 2012. Mechanics of stretchable electronics and soft machines. MRS Bull. 37 (3), 218–225.
Suo, Z.G., Zhao, X.H., Greene, W.H., 2008. A nonlinear field theory of deformable dielectrics. J. Mech. Phys. Solids 56 (2), 467–486.
Suo, Z.G., 2010. Theory of dielectric elastomers. Acta Mech. Solida Sin. 23 (6), 549–578.
Toupin, R.A., 1956. The elastic dielectric. J. Rational Mech. Anal. 5 (6), 849–915.
Trivedi, D., Rahn, C.D., Kier, W.M., Walker, I.D., 2008. Soft robotics: biological inspiration, state of the art, and future research. Appl. Bionics Biomech. 5 (3), 99–117.
Usmani, S.A., Beatty, M.F., 1974. On the surface instability of a highly elastic half-space. J. Elast. 4, 249–263.
Wang, B.Y., Krause, S., 1987. Properties of dimethylsiloxane microphases in phase-separated dimethylsiloxane block copolymers. Macromolecules 20, 2201–2208.
Wu, B., Su, Y.P., Chen, W.Q., Zhang, C.Z., 2017. On guided circumferential waves in soft electroactive tubes under radially inhomogeneous biasing fields. J. Mech. Phys. Solids 99, 116–145.
Wu, J., Kim, S., Chen, W.Q., Carlson, A., Hwang, K.-C., Huang, Y.G., Rogers, J.A., 2011. Mechanics of reversible adhesion. Soft Matter 7 (18), 8657–8662.
Wu, Y.F., 2012. Indentation Analysis of Piezoelectric Materials and Quasicrystals. Zhejiang University, Hangzhou, China.
Yam, C.-M., Xiao, Z.D., Gu, J.H., Boutet, S., Cai, C.Z., 2003. Modification of silicon AFM cantilever tips with an oligo(ethylene glycol) derivative for resisting proteins and maintaining a small tip size for high-resolution imaging. J. Am. Chem. Soc. 125 (25), 7498–7499.
Yang, F.Q., 2006. Effect of adhesion energy on the contact stiffness in nanoindentation. J. Mater. Res. 21 (10), 2683–2688.
Zhang, M.G., Cao, Y.P., Li, G.Y., Feng, X.Q., 2014. Spherical indentation method for determining the constitutive parameters of hyperelastic soft materials. Biomech. Model. Mechanobiol. 13 (1), 1–11.
Zhang, Q., Li, H., Poh, M., Xia, F., Cheng, Z., Xu, H., Huang, C., 2002. An all-organic composite actuator material with a high dielectric constant. Nature 419, 284–287.
Zhang, W.L., Qian, J., Chen, W.Q., 2012. Indentation of a compressible soft electroactive half-space: some theoretical aspects. Acta Mech. Sin. 28 (4), 1133–1142.
Zhao, X.H., Suo, Z.G., 2007. Method to analyze electromechanical stability of dielectric elastomers. Appl. Phys. Lett. 91, 061921.
Zheng, Y., Crosby, A.J., Cai, S., 2017. Indentation of a stretched elastomer. J. Mech. Phys. Solids 107, 145–159.
Zhu, R.K., Ming, W.J., Liu, Y.Y., Pan, K., Lei, C.H., 2018. The intrinsic piezoresponse in piezoelectric medium under contact-mode piezoresponse force microscopy. Int. J. Mech. Sci. 145, 400–409.
Zisis, T.h., Zafiropoulou, V.I., Giannakopoulos, A.E., 2011. The adhesive contact of a flat punch on a hyperelastic substrate subject to a pull-out force or a bending moment. Mech. Mater. 43, 1–24.
Zisis, T.h., Zafiropoulou, V.I., Giannakopoulos, A.E., 2015. Evaluation of material properties of incompressible hyperelastic materials based on instrumented indentation of an equal-biaxial prestretched substrate. Int. J. Solids Struct. 64–65, 132–144.